

Spring 2017

Two Topics in Astrophysics: Exoplanetary Gravitational Microlensing and Radio Interferometry

Eleanor Sara Turrell
Bard College

Follow this and additional works at: https://digitalcommons.bard.edu/senproj_s2017



Part of the [Cosmology, Relativity, and Gravity Commons](#), and the [Instrumentation Commons](#)



This work is licensed under a [Creative Commons Attribution-Noncommercial-No Derivative Works 4.0 License](#).

Recommended Citation

Turrell, Eleanor Sara, "Two Topics in Astrophysics: Exoplanetary Gravitational Microlensing and Radio Interferometry" (2017). *Senior Projects Spring 2017*. 158.
https://digitalcommons.bard.edu/senproj_s2017/158

This Open Access work is protected by copyright and/or related rights. It has been provided to you by Bard College's Stevenson Library with permission from the rights-holder(s). You are free to use this work in any way that is permitted by the copyright and related rights. For other uses you need to obtain permission from the rights-holder(s) directly, unless additional rights are indicated by a Creative Commons license in the record and/or on the work itself. For more information, please contact digitalcommons@bard.edu.

Two Topics in Astrophysics: Exoplanetary Gravitational Microlensing and Radio Interferometry

A Senior Project submitted to
The Division of Science, Mathematics, and Computing
of
Bard College

by
Eleanor Turrell

Annandale-on-Hudson, New York
May, 2017

Abstract

My project naturally divides itself into two parts, both aiming to increase our understanding of the sky by gleaning information about objects that surround our Earth. The first section explores gravitational microlensing as an exploration technique for exoplanets. When a massive object passes in front of a distant star, the light emanating from the star is shifted due to the gravity of the massive object. This shift of light is observed as a momentary spike in the brightness of the distant star and is called a microlensing event. While monitoring the brightness in time of a distant star, a microlensing event is occasionally observed. The nature of the spike can give insight into the lensing mass. I am specifically interested in identifying when planets outside of our solar system, exoplanets, act as gravitational lenses. I have modeled magnification in time graphs, also known as light-curves, indicative of different categories of exoplanetary microlensing events. The varieties I have modeled include single lens, binary lens, and triple lens configurations and also finite source effects.

In conjunction, I constructed a 20-foot radio interferometer designed to measure the diameter of the Sun. An interferometer system is used to efficiently increase the collection area of an antenna. The structure consists of a 20-foot ladder mounted on a plywood structure that facilitates latitudinal and azimuthal movement. Once the 10-13 GHz radio signal has been collected and directed onto an antenna, the electronic equipment displays the signal as a direct current.

Contents

Abstract	iii
Dedication	ix
Acknowledgments	xi
Introduction	1
1 Gravitational Microlensing	9
1.1 Gravitational Lensing	9
1.1.1 A Newtonian Derivation of the Deflection Angle	11
1.2 Gravitational Microlensing	13
1.2.1 Perfect Alignment Lensing	13
1.2.2 A Short Poem About the Sky Being Small	15
1.3 Notation	15
1.3.1 Moving into the Complex Plane	15
1.4 Two Techniques for Obtaining Total Magnification Equation	18

1.4.1	Total Magnification from Summation of Image Magnifications . . .	18
1.4.2	Resultant Method to Eliminate Dependence on Image Position . . .	19
1.5	Time Parameterization of Star Position	20
2	Modeling Light Curves for Exoplanetary Microlensing Events	23
2.1	Single Lens	24
2.1.1	Single Lens Magnification from the Summation of Image Magnifications	24
2.1.2	Single Lens Light Curve	25
2.1.3	Single Lens with a Finite Star Size	27
2.2	Double Lens	31
2.2.1	Double Lens Magnification from the Summation of Image Magnifications	31
2.2.2	Double Lens Total Magnification using Resultant Method	32
2.2.3	Double Lens Light Curves	33
2.3	Triple Lens	35
2.3.1	Triple Lens Total Magnification using Resultant Method	35
2.4	Future Goals	37
3	Radio Interferometry	39
3.1	Overview of Radio Interferometry	40
3.2	Interferometer Construction	45
3.2.1	Materials List	45
3.2.2	Methods	46
3.3	Adjusting Radio Signal	51
3.3.1	Materials List	51
3.3.2	Methods	52

4 The Signal	59
4.1 Radio Emission of The Sun	59
4.2 Testing the Signal	64
4.3 Future Goals	65
Bibliography	67
.1 One Lens Light Curve from Image Positions	70
.2 One Lens Finite Source	72
.3 Double Lens	74
.4 Triple Lens	76

Dedication

To subjectivity, indulgence and all things feminine.

Acknowledgments

I would like to acknowledge my family who always demanded I take my interests seriously. I would like to thank my friends, especially Duncan Routh and Maia Weisenhaus, and my advisors Hal Haggard, Eleni Alexandra-Kontou and Richard Murphy for helping me to find those interests, then challenging and caring for me along the way.

Introduction

The study of stars can be traced back to the origins of record keeping, the genesis of scientific inquiry. Ancient Babylonian civilizations left behind stone tablets describing a detailed trajectory of the Sun throughout a year. By 2000 B.C., Babylonians had divided each year into twelve sections and established a calendar similar to our modern calendar [6]. The Greek civilization expanded their inquiries of the expansive dome above us. Greek scientists, mystics, and priests shifted from the Sun and began speculating about other planets in our solar system. While they were convinced that earth was the central point of our solar system, much of their documentation of the sky was incredibly thorough and precise [6]. Astronomical inquiry proceeded as science typically does; an expansive lull of fifteen hundred years followed by rapid invention and development. Beginning in the 17th century, our current paradigm of astronomical inquiry emerged. As a result of the invention of the telescope and a surge of mathematical discovery, scientist such as Kepler, Copernicus, Newton, and Galileo discerned a model of our solar system with dramatically more evidence, accuracy, and mathematical precision.

In the early 1900's, scientists measured Doppler-shifted spectral lines to determine the velocities of galaxies. In 1915, scientist V.M. Slipher [19] revealed the surprising

result that all but one of the 12 galaxies he had examined showed redshifting. This meant the galaxies were rapidly traveling away from Earth and diverging from one another. Meanwhile, Hubble cataloged stars and galaxies based on their spatial separation and velocity. Combining his results with data from Slipher, Hubble recognized a galaxy's velocity, v , was related directly to its distance, d , by the Hubble Constant H_0 . He coined this relationship as Hubble's Law [21]. The discovery implied the fanciful idea that the universe was expanding into an uncharted abyss. Coincidentally, in 1917 theorist Willem de Sitter had developed a model of an expanding Universe based on Einstein's Theory of General Relativity [20]. His theory predicted a red shift that increased with distance and was held in conjunction with empirical as support for general relativity [9].

General relativity posits that the distribution of masses in space set up a gravitational topography that instructs the behavior of other masses. Einstein's theory, formally developed in 1916, is true for all masses in space, but the effects are most apparent for enormous masses at least the size of our Sun. In the coming years, general relativity would prove to be difficult to experience and equally difficult to prove through observation.

In 1920, Eddington [16] recognized a potential to observe gravitational lensing, an idea that could provide the first proof of general relativity. In his theory, background starlight could be deflected by the gravitational effect a foreground mass has on the space-time surrounding it. He correctly postulated that a lensed star would be seen as two images. Following publications by Einstein [14] and Zwicky [15] detailing how a gravitational lensing observation would appear, this test of General Relativity became an experimental reality.

In time, gravitational lensing surfaced as the most available proposal to observe general relativity. Binary stars are common and might be difficult to distinguish between two lensed images, and the two images of a binary star. Two lensed images would be nearly identical which could not happen with a binary star. The two images would appear with

magnified brightness. And also, lensing acts as a natural telescope, making the images more possible to resolve. In 1979, Walsh, Carswell, and Weymann [17] observed multiple images of the high redshift quasar Q0957+561 lensed by a foreground galaxy [17]. The observation served as evidence for general relativity and was used to estimate the Hubble constant within $17\text{kms}^{-1}\text{Mpc}^{-1}$.

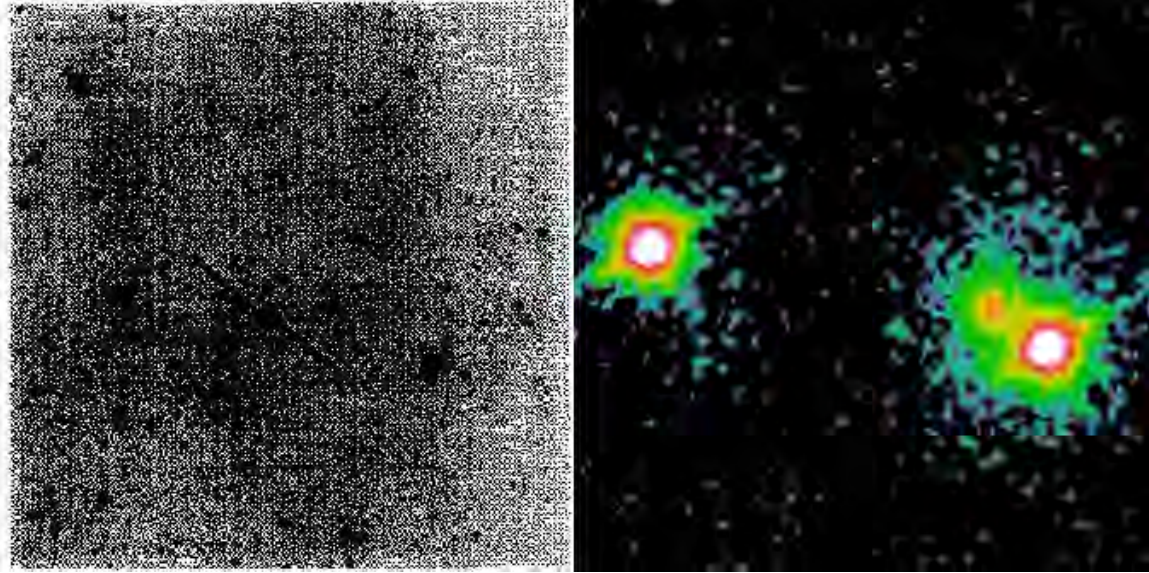


Figure 0.0.1: These images show the first observed quasar Q0957+561. The finding graph was the original data used as evidence for the lensing event. The image is 8.5 arc min squared obtained by the Palomar Observatory Sky Survey [17]. The image on the right was created from an observation of the same lensing by *Hubble Space Telescope* in 1995 [8].

Gravitational lensing exploded as a new exploration technique. Gravitational lensing was found to unveil details about the rate at which the Universe expands, the presence of dark matter, orbital motion of galaxies and, most importantly to me, identification and classification of exoplanets.

Gravitational microlensing is a specific type of gravitational lensing that occurs when multiple images of a background star, also known as a source star are created. The images are too close together to be resolved and instead appear as one image with a strongly increased brightness. Microlensing became an active area of study in 1986

following a paper by Paczynski [10]. Surveys searching for microlensing events began in the early 1990's and already thousands of events have been observed [2]. The first searches were intended to discover a halo of dark matter in the Magellanic Clouds [10].

In 1995, microlensing surveys began searching for exoplanets using an array of telescopes throughout the southern hemisphere. Gravitational microlensing is used to study separations of binary masses, determine the mass of foreground masses and determine the size of distant stars [18]. Gravitational Microlensing is one of five popular techniques used to discover exoplanets along with transit, direct imaging, astrometry, and radial velocity observations.¹ The main advantage of microlensing is the elusive parameter space it can explore. Microlensing is sensitive to low-mass planets outside the snow line, the region of a solar system's protoplanetary disk where water can be found in its solid state. In his review of exoplanetary microlensing, Dr. B. Scott Gaudi explains, "microlensing surveys can potentially yield a complete picture of the demographics of essentially all planets with masses greater than that of Mars" [2].

Gravitational microlensing is also especially attuned to circumbinary systems. A circumbinary system refers to a system where one planet revolves around a binary star system. Approximately 10% of binary star systems appear to have planets, similar to the prevalence of exoplanets in single star systems. Despite these benefits, searching for exoplanets using gravitational microlensing requires demanding analysis of collected light curves. Although efforts began in 1995, the first convincing exoplanet detection did not materialize for almost a decade, in 2003 [26].

Amongst the excitement of the first exoplanet citing, OGLE and MOA collaborations upgraded their observing equipment and began to recognize microlensing as a

¹A simplified but illuminating animation showing microlensing can be found at NASA's website by following the link <https://exoplanets.nasa.gov/interactable/11/>

viable avenue toward discovering exoplanets. According to NASA, forty-four exoplanets have been found using gravitational microlensing².

Chapter One of my project describes the theoretical background of microlensing in greater detail and Chapter Two details my efforts to model exoplanetary gravitational microlensing with the goal of locating and determining the mass of an exoplanet based on its effect on the observed light over time from the distant star, from here forward referred to as the distant star's light curve.

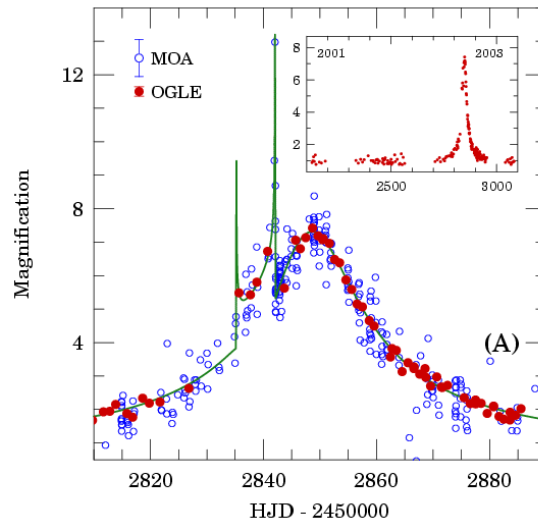


Figure 0.0.2: The light curve of the first exoplanet identified via gravitational microlensing. If the star was a main sequence primary, the lens is approximated to be 1.5 Jupiter masses. The event lasted 120 seconds, and more information regarding the time scale of this image can be found in a paper by I.A. Bond detailing the observation [26].

The second half of my project undertakes a different attempt to probe the Universe, this time using radio interferometry. In the late 1920's, around ten years after Hubble began mapping the Universe as an expanding container, it was realized that radio could be used in astronomy. In 1930, Karl Jansky noticed a regular pattern within the noise interfering with radio communication of Bell Telephone Laboratories. Jansky began compiling data about this peculiar noise using an antenna mounted on a marry-go-round

²cite (<https://exoplanets.nasa.gov/> that also offers a helpful graphic explaining microlensing

(Smith and carr II). He recognized that the noise traveled from east to west during the day and eventually “obtained enough data about this hiss or ‘radio noise’ to show that it had an origin. . . fixed among the stars” [6]. For the first time, it was realized that extraterrestrial radio sources existed. We now know that radio emissions run rampant throughout the Universe and offer a vastly different picture than visible light alone. Our Sun, Jupiter, and the cosmic microwave background are well known radio emitters [6].

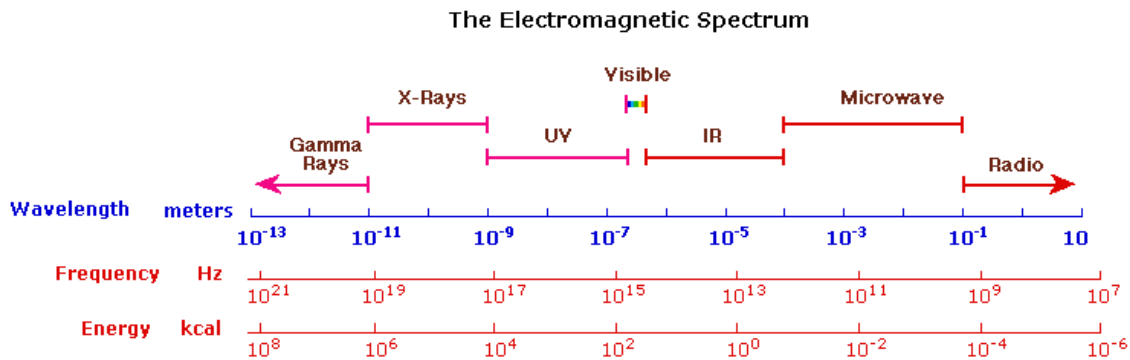


Figure 0.0.3: Radio waves make up the zone of electromagnetic spectrum that have the lowest wavelengths and highest frequencies. More information regarding the origins of radio emissions from our Sun can be found in Section 4.1. This basic figure of the electromagnetic spectrum was created by William Reusch [27]

World War II delivered another surge in scientific invention with monumental developments in radio communications. While experts were distracted by wartime requirements, amateur astronomers were at the forefront of intergalactic radio research. In 1943, Grote Reber first discovered solar radio emission using his 31-foot parabola (Smith and Carr 5). Astronomers appreciated radio’s ability to collect reliable data independent of cloud cover or time of day. While collecting radio signal under all weather conditions, they began to appreciate those details of the universe uniquely available to radio data. We now know that radio emissions run rampant throughout the Universe and offer a vastly different picture than visible light alone. Fixtures prominent in the visual spectrum suddenly disappear and give way to different features in the radio spectrum. For example, “the radio sun is highly variable...[and its total brightness has been known to increase]a

thousand-fold in the matter of seconds during violent eruptions” [6]. Our Sun, Jupiter, exploding stars and the cosmic microwave background are well known radio emitters [6].

Many of these radio sources can be investigated with relatively unspecialized and inexpensive radio technology. Along this line, I have constructed a twenty-foot radio interferometer to collect radio waves emitted by our sun in order to determine its diameter. Interferometry is used in astronomy to combine signal collected by two or more elements. The resolution of an interferometer is directly related to the separation distance between the elements, and the setup leads to higher resolution capabilities than a single element telescope [4]. This section of my project begins in Chapter ?? where I describe the benefits of an interferometer, my building process and general specifications of my contraption. In Chapter 4 I explore the Sun’s radio emissions, progress in testing my interferometer along with future construction goals.

1

Gravitational Microlensing

1.1 Gravitational Lensing

Gravitational lensing was initially respected as proof of general relativity. While the intricate details of the general relativistic effects causing gravitational lensing are beyond the scope of my project, the general idea is straightforward. Mass is distributed in a non-uniform way throughout the universe, coagulating into planets, stars, pulsars, then dispersing into void for long stretches. Each mass propagates a gravitational field that exerts a force on other masses in the vicinity.

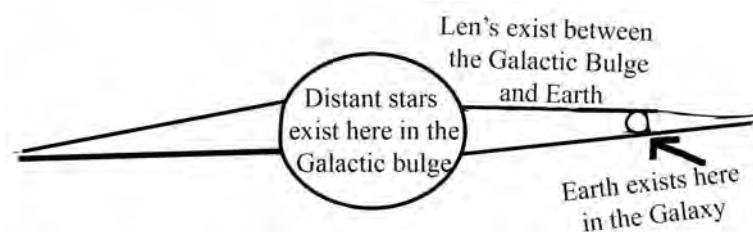


Figure 1.1.1: This diagram shows relative locations of star, lens, and Earth in the context of our galaxy.



Figure 1.1.2: These paintings depict gravitational lensing events. On the left, the dark spot in the middle is a mass passing in front of a distant star. The mass behaves like a lens creating two identical images of the star. On the right, the mass is perfectly aligned with the distant star which causes the images to connect into a ring. This ring is referred to as the Einstein ring. The radius of the Einstein ring is determined by the mass of the lens. These two paintings by Jon Lomberg can be found in Stephen Hawking's novel *An Illustrated Theory of Everything* [28].

The arrangement, synthesis and superposition of the gravitational force of various masses creates spacetime. When considering every mass in the universe, spacetime becomes a complicated contour map full of bends, folds and organic curves.

If a distant star is situated in the galactic bulge (see Figure 1.1) the path between the star and Earth is riddled with masses and complicated spacetime. As light travels from the star toward Earth it follows the curved spacetime. From the point of view of the Earth, this path appears bent and contorted. When light passes by larger masses, the deviations from a straight path are more distinct. These enormous masses act as gravitational lenses, and it appears that there are multiple images of the star. Brightness of the images is conserved. Therefore, when multiple images of the star are created, the observed brightness is severely increased. On a graph of a stars brightness in time, called the light curve of the star, a gravitational lensing event appears as a monumental peak.

1.1.1 A Newtonian Derivation of the Deflection Angle

While gravitational lensing is an exclusively general relativistic prediction, the deflection caused by the lensing mass can be approximated using a Newtonian model. The situation can be approximated as a particle moving at the speed of light being deflected by a larger mass. In the figure below we use the small angle approximation to pretend the light travels in a straight line, bends at one instant and then continues to travel in a straight line in the new direction.

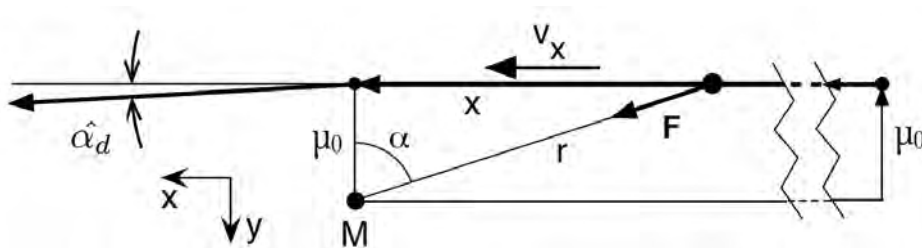


Figure 1.1.3: This diagram shows the deflection of light for the Newtonian approximation where light is treated as a very fast particle. This image originally appears in *Spacetime Physics* by Wheeler and Taylor [3].

Suppose the particle initially moves in the x -direction and the deflection is very small and occurs entirely at the closest approach as shown in Figure 1.1.3 Integrating Newton's second law in the y -direction gives

$$F_y = \frac{dp_y}{dt} \Rightarrow \int F_y dt = \Delta p_y \Rightarrow \int F_y dt = m\Delta v_y. \quad (1.1.1)$$

According to Newton's law of gravitation the y -component of the force is

$$F_y = F \cos \alpha = \frac{GMm}{r^2} \cos \alpha. \quad (1.1.2)$$

We want to change the integral of Equation (1.1.1) to be over the angle α

$$v_x = \frac{dx}{dt} \Rightarrow dt = \frac{dx}{v_x} \approx \frac{dx}{c}, \quad (1.1.3)$$

where we used the approximation $c = \sqrt{v_x^2 + v_y^2} \approx v_x$ because the deflection is very small. From Figure 1.1.3 we see that

$$x = \mu_0 \tan \alpha \Rightarrow dx = \frac{\mu_0}{\cos^2 \alpha} d\alpha, \quad (1.1.4)$$

where μ_0 is the impact parameter. Also from Figure 1.1.3 we have that

$$r = \frac{\mu_0}{\cos \alpha}. \quad (1.1.5)$$

Using Equations (1.1.2) - (1.1.5) and putting them into Equation (1.1.1) gives

$$\int_{-\pi/2}^{\pi/2} \frac{GMm \cos \alpha}{\mu_0 c} d\alpha = m \Delta v_y \Rightarrow \Delta v_y = \frac{2GM \cos \alpha}{\mu_0 c}, \quad (1.1.6)$$

where I used the fact that the angle α goes from $-\pi/2$ to $\pi/2$ as the light ‘particle’ passes by the lens. Since the deflection angle is tiny, $\sin \theta_{\text{defl}} \approx \theta_{\text{defl}}$ and

$$\hat{\alpha}_d \approx \frac{\Delta v_y}{c} = \frac{2GM}{\mu_0 c^2}. \quad (1.1.7)$$

While derived very differently, the General Relativistic result differs only by a factor of 2 and

$$\hat{\alpha}_d = \frac{4GM}{\mu_0 c^2}. \quad (1.1.8)$$

1.2 Gravitational Microlensing

1.2.1 Perfect Alignment Lensing

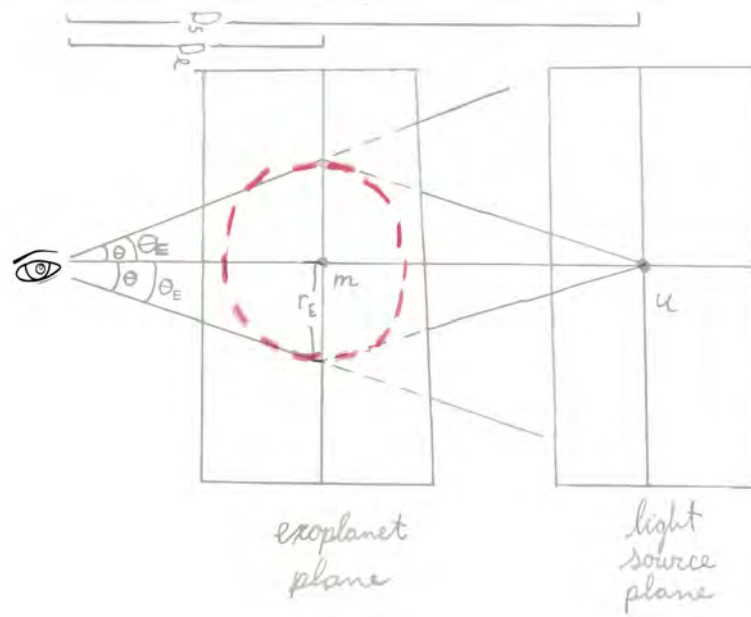


Figure 1.2.1: This shows gravitational lensing with a single lens in a perfectly alignment across multiple planes. The lens is located at position m , unrelated to any variables used in the previous section. The star is located at position u .

Figure 1.2.1 shows the lensing phenomenon from Section 1.1.1 in multiple planes in the sky. Light emitted from a distant star located at position u is lensed by a mass at position m (which has no reference to any variables used in Section 1.1.1). The star is positioned directly behind the lens. This arrangement occurs when $\beta = 0$, which causes $\theta = \theta_E$. The variable r_E is the Einstein radius, θ_E is the angular description of the Einstein radius, and the red dashed line is termed the Einstein ring [2]. The total mass of a lens determines the Einstein radius. This figure also shows a useful substitution. Replacing r_E with $D_l \sin \theta$ and using the small angle approximation ¹ to estimate $\sin \theta \approx \theta$, the Einstein radius can be determined by

$$r_E \approx D_l \theta. \quad (1.2.1)$$

¹Since the distance between lens and source is always large the small angle approximation always applies.

During a lensing event, a distant star is imagined to travel in a fixed trajectory behind a lens². As the star passes behind the lens, the images that are created shift ever so slightly around the Einstein radius. The images are shown as small blue crescents in Figure 1.2.1. The lens itself is only a minuscule unresolvable speck of light and the images are not distinguishable from one another. They appear stacked on top of each other. Instead of being observed as copies of the same image, as in Figure 1.1.2, they appear as one image with increased brightness.

A caustic is the position of the star (in the star plane) where the images merge together. When a point star is located on the caustic, a spike of infinite brightness is seen on the light curve. Caustics will be important to interpreting the light curves in Chapter 2. For the single lens case, the caustic is a single point, the location of the lens projected onto the star plane. The caustic curve for a two lens system will be discussed in Section 2.2.3.

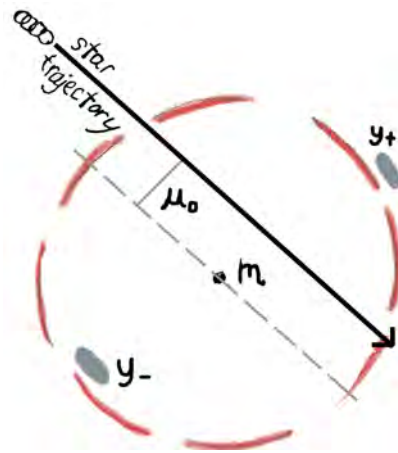


Figure 1.2.2: Light emitted by the star is lensed by mass m and appears as two images around the Einstein radius. Image position's are often normalized to the Einstein radius.

Every star has a finite size but can be approximated as a point mass. Throughout the project it will be occasionally useful to imagine the unrealistic existence of a point

²In fact, every mass in the system is moving in relation to the others. Since only relative motion matters, it is reasonable to consider the lens as stationary and set the distant star along a trajectory in time. Details about this trajectory and its impact on the final light curve can be found in Section 1.5.

star. When the distant star is approximated to be a point star, the the light curve can display periods of infinite magnification. A compact point mass is not likely to be observed in nature and a fully illuminated Einstein ring of infinite magnification cannot be either. While a point mass approximation is often useful, it is important to realize this is not a realistic situation.

1.2.2 A Short Poem About the Sky Being Small

When did the sky get so small?

Blue skies don't end but that blue sky sets
to reveal a milli little specks
too small, they're barely distinguishable at all

1.3 Notation

1.3.1 Moving into the Complex Plane

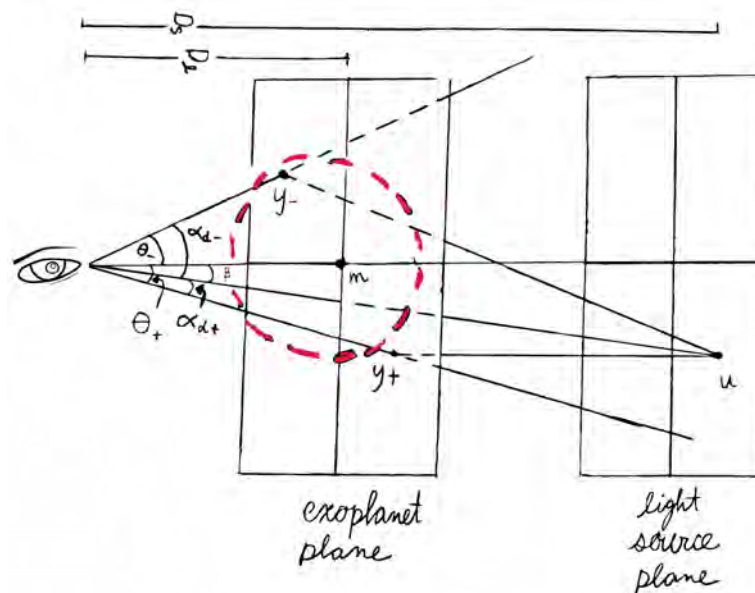


Figure 1.3.1: This diagram shows lensing when the star and lens are not perfectly aligned.

Table 1.3.1: A collection of many of the important variables shown in Figure 1.3.1

u	position of source
y_{\pm}	position of images
m	position of lens
β	angular position of source
θ_{\pm}	angular position of images
$\alpha_{d_{\pm}}$	defined by relationship $\beta = \pm\theta_{\pm} \mp \alpha_{d_{\pm}}$
$\hat{\alpha}_{d_{\pm}}$	angle between source and image with vertex at lens position (not on Figure 1.3.1)

From Figure 1.2.1 and Figure 1.3.1, the relation

$$\beta = \theta - \alpha_d \quad (1.3.1)$$

is obvious. This relation is called the lens equation. Using trigonometric relationships, I will adjust the lens equation into a more useful form. If

$$\hat{\alpha}_d(D_s - D_l) = \alpha_d D_s, \quad (1.3.2)$$

$$\alpha_d = \left(\frac{D_s - D_l}{D_s} \right) \hat{\alpha}_d. \quad (1.3.3)$$

Replacing $\hat{\alpha}_d$ from Equation (1.1.8), α_d in terms of θ , D_s , D_l and constants becomes

$$\alpha_d = \frac{4GM}{(D_l\theta)c^2} \left(\frac{D_s - D_l}{D_s} \right). \quad (1.3.4)$$

To make this equation function for N_L lenses with masses m_i and angular positions from the observer $\theta_{\mathbf{m},i}$, Equation (1.3.4) becomes a sum. The preferred form of the lens equation shown in Equation (1.3.6) isn't directly derivable from Equation (1.3.1). By making a couple very reasonable assumptions the general idea can be followed; the point lenses are near each other in relation to distances D_l and D_s and the point lenses are stationary in comparison to light moving at velocity c . Under these assumptions where

$$D_{rel} \equiv (D_l^{-1} - D_s^{-1})^{-1}, \quad (1.3.5)$$

$$\boldsymbol{\alpha}_d = \frac{4G}{D_{rel}c^2} \sum_i^{N_L} m_i \frac{\boldsymbol{\theta} - \boldsymbol{\theta}_{m,i}}{|\boldsymbol{\theta} - \boldsymbol{\theta}_{m,i}|^2}. \quad (1.3.6)$$

The derivation of Equation (1.3.6) also requires including a time delay function to include how magnification varies dependent on factors other than position of the star [2]. The time delay is due to the different path lengths of deflected photons and is beyond the scope of my project. The dependence results from the distance between star and lens, and has been used to glean details about the Hubble constant [12].

Placing α_d from Equation (1.3.6) into the lens equation gives

$$\beta = \theta - \frac{4G}{D_{rel}c^2} \sum_{i=1}^{N_L} m_i \frac{\boldsymbol{\theta} - \boldsymbol{\theta}_{m,i}}{|\boldsymbol{\theta} - \boldsymbol{\theta}_{m,i}|^2}. \quad (1.3.7)$$

When moving to more than one lens, it is also helpful to write the star and lens positions as complex numbers. This way, two dimensions can be described using one number and taking the conjugate access both pieces of information. Below is a chart to outline these notational conventions. Notice that u and y are normalized to the Einstein radius.

Table 1.3.2: This chart clearly displays the variables used in lens Equation (1.3.8).

	normalized angular position	dimensionless complex coordinates	two dimensional complex position
Star	$\mathbf{u} \equiv \frac{\beta}{\theta_E}$	$\mathbf{u} = (u_1, u_2)$	$\zeta = (u_1 + iu_2)$
Image	$\mathbf{y} \equiv \frac{\boldsymbol{\theta}}{\theta_E}$	$\mathbf{y} = (y_1, y_2)$	$z = (y_1 + iy_2)$

Using two dimensional complex notation for source and lens position and defining $\bar{z}^{-1} \equiv \frac{z}{|z|^2}$ the lens equation becomes

$$\zeta = z - \sum_i^{N_L} \frac{\epsilon_i}{\bar{z} - \bar{z}_{m,i}}. \quad (1.3.8)$$

This equation allows for relating image position to star position and is the starting point for creating any light curve.

1.4 Two Techniques for Obtaining Total Magnification Equation

I have used two main techniques to find an equation for total magnification dependent on star position. In this section I will describe both techniques, then in Chapter 2 I will develop the methods with further specificity creating the light curves.

1.4.1 Total Magnification from Summation of Image Magnifications

My first technique is to locate each image, find the magnification of each image, and then sum the magnifications to find the total magnification. Equation (1.3.8) can provide all image positions for any system with N lenses [2]. While lensing conserves brightness, the angular area of the source is not the same as the angular area of the image. The flux is defined as the area times the surface brightness and it is different for the image and the source. Thus the magnification of each image A_j is defined as the ratio of the total area of the image to the total area of the star. The magnification of each image is given by

$$A_j = \frac{1}{\det J} \Big|_{z=z_j}, \quad (1.4.1)$$

where

$$\det J \equiv \begin{vmatrix} \partial u_1/\partial y_1 & \partial u_1/\partial y_2 \\ \partial u_2/\partial y_1 & \partial u_2/\partial y_2 \end{vmatrix} = \frac{\partial u_1}{\partial y_1} \frac{\partial u_2}{\partial y_2} - \frac{\partial u_1}{\partial y_2} \frac{\partial u_2}{\partial y_1}. \quad (1.4.2)$$

In gravitational lensing $\partial u_1/\partial y_2 = \partial u_2/\partial y_1$ because of symmetry [1] and the derivatives can be written as

$$d\zeta = \frac{\partial \zeta}{\partial z} dz + \frac{\partial \zeta}{\partial \bar{z}} d\bar{z} = \left(\frac{\partial \zeta}{\partial z} + \frac{\partial \zeta}{\partial \bar{z}} \right) dy_1 + i \left(\frac{\partial \zeta}{\partial z} - \frac{\partial \zeta}{\partial \bar{z}} \right) dy_2 \quad (1.4.3)$$

and

$$\begin{aligned} d\zeta &= du_1 + i du_2 = \frac{\partial u_1}{\partial y_1} dy_1 + \frac{\partial u_1}{\partial y_2} dy_2 + i \left(\frac{\partial u_2}{\partial y_1} dy_1 + \frac{\partial u_2}{\partial y_2} dy_2 \right) \\ &= \left(\frac{\partial u_1}{\partial y_1} + i \frac{\partial u_2}{\partial y_1} \right) dy_1 + \left(\frac{\partial u_1}{\partial y_2} + i \frac{\partial u_2}{\partial y_2} \right) dy_2. \end{aligned} \quad (1.4.4)$$

Using Equations (1.4.3) and (1.4.4) I get

$$\frac{\partial \zeta}{\partial z} + \frac{\partial \zeta}{\partial \bar{z}} = \frac{\partial u_1}{\partial y_1} + i \frac{\partial u_2}{\partial y_1}, \quad (1.4.5a)$$

$$\frac{\partial \zeta}{\partial z} - \frac{\partial \zeta}{\partial \bar{z}} = \frac{\partial u_2}{\partial y_2} - i \frac{\partial u_1}{\partial y_2}. \quad (1.4.5b)$$

Solving for the derivatives of ζ and squaring gives

$$4 \left(\frac{\partial \zeta}{\partial z} \right)^2 = \left(\frac{\partial u_1}{\partial y_1} + \frac{\partial u_2}{\partial y_2} \right)^2, \quad (1.4.6a)$$

and

$$4 \frac{\partial \zeta}{\partial \bar{z}} \frac{\partial \bar{\zeta}}{\partial \bar{z}} = \left(\frac{\partial u_1}{\partial y_1} - \frac{\partial u_2}{\partial y_2} \right)^2 + 4 \left(\frac{\partial u_2}{\partial y_1} \right)^2. \quad (1.4.7a)$$

Subtracting the previous equations gives the expression for the determinant of the Jacobian as given in Eq. (1.4.2), so we can write

$$\det J = \left(\frac{\partial \zeta}{\partial z} \right)^2 - \frac{\partial \zeta}{\partial \bar{z}} \frac{\partial \bar{\zeta}}{\partial \bar{z}}. \quad (1.4.8)$$

If we don't have continuous mass density, like in the case of lenses that can be approximated by point masses $\partial \zeta / \partial z = 1$ (see reference [1] for details) so Equation (1.4.8) becomes

$$\det J = 1 - \frac{\partial \zeta}{\partial \bar{z}} \frac{\partial \bar{\zeta}}{\partial \bar{z}}. \quad (1.4.9)$$

To find the total magnification we simply add the absolute values of the magnifications of all the images

$$A \equiv \sum_j |A_j|. \quad (1.4.10)$$

1.4.2 Resultant Method to Eliminate Dependence on Image Position

As I moved toward more lenses, the lens equation grew immensely in complexity. Finding the image locations for two lenses requires solving a fifth order polynomial. While

the fifth order polynomial is solvable numerically, a configuration with more lenses provides a larger polynomial that may not be. I needed the total magnification as a function of star position but finding the position of each image is not especially useful and circumventing this step is computationally faster.

An article by Witt and Moa [1] detailed a method where they eliminated the dependence on image position to produce an equation for the total magnification as a function of star position. This method requires building two messy polynomials in z , the image position, then taking the resultant of these two polynomials to eliminate the z dependence. It is then possible to solve for total magnification as a function of star position. The difficult part was obtaining the two polynomials in z , then the method is quite straight forward. This method is employed in Section 2.2 for two lenses and developed in Section 2.3 for three lenses.

1.5 Time Parameterization of Star Position

Once the total magnification has been found as a function of star position, star position can be made a function of time. When searching for a microlensing event, the flux of a distant star is monitored for days, weeks, or months. When a microlensing event occurs, the impact parameter is very near zero, so the time of the event is very short. Because of this, I make the assumption that the star follows a linear trajectory behind the lens during the event. When only looking at a very small portion of the star's trajectory the path will appear as a straight line. I will plot a model light curve, a Magnification vs. Time graph that assumes the star travels in uniform, rectilinear motion behind a lens. The relative lens-source motion in time can be parameterized by

$$u(t) = \left[\mu_0^2 + \left(\frac{t - t_0}{t_E} \right)^2 \right]^{1/2}, \quad (1.5.1)$$

where μ_0 is the minimum separation of lens and star when looking at the system in a one dimensional plane, (see Figure 1.2.1), normalized to the Einstein radius. The time of maximum magnification is t_0 , and

$$t_E \equiv \frac{\theta_E}{\mu_{rel}}, \quad (1.5.2)$$

represents the time for the proper motion of the star to cross the Einstein radius.

I have collected the time dependence into one variable,

$$T \equiv \left(\frac{t - t_0}{t_E} \right). \quad (1.5.3)$$

Using the condensed variable T , the magnification vs. time graph will be a smooth symmetric ‘‘Paczynski curve.’’ In the final magnification equation I make star position a function of time by replacing

$$u \rightarrow \sqrt{\mu_0^2 + T^2}. \quad (1.5.4)$$

2

Modeling Light Curves for Exoplanetary Microlensing Events

This chapter describes lensing events and my models of the light curves you would expect to observe in microlensing. Where the previous chapter aimed to provide a comprehensive understanding of the theory, this chapter is more practically driven toward creating light curves. The general structure was to develop a sound method with one lens, then revise the method to function for two lenses and beyond. Often, this expansion into more lenses added new considerations and required adjustments or a new approach. The theory provided in this chapter is intended to show the bare bones of what is necessary to follow the Mathematica files provided in the Appendix (and online¹) and understand how the following light curves have been created. For a more comprehensive overview of modeling light curves, refer to the 2012 microlensing summary written by Scott Gaudi [2] and other references made throughout this chapter.

¹at bohr.physics.berkeley.edu/hal/projects/eturrell

2.1 Single Lens

2.1.1 Single Lens Magnification from the Summation of Image Magnifications

I will first apply this method to the single lens system. A copy of the Mathematica files showing these steps can be found in Appendix .1. Applying the method described in Section 1.4.1 requires some adjustment. For the single lens case I have used the variable u for image position and the variable y for lens positions to indicate that these are real numbers in a one-dimensional real plane. The variable A is used for magnification. By taking the sum over a single lens, that is $N_L = 1$, Equation (1.3.8) simplifies to

$$u = y - y^{-1}, \quad (2.1.1)$$

which can be written as the quadratic equation

$$y^2 - uy - 1 = 0. \quad (2.1.2)$$

This has two solutions, two image positions, at

$$y_{\pm} = \pm \frac{1}{2}(\sqrt{u^2 + 4} \pm u). \quad (2.1.3)$$

While the brightness of each image is conserved (by Liouville's Theorem), the solid angle of the star is changed due to lensing. The magnification can be found by finding the ratio between the total area of the images and the total area of the star. Each image is distorted, elongated tangentially by y_{\pm}/u and compressed radially by dy_{\pm}/du .

The inverse of the determinant of the Jacobian of the lens equation can be immensely simplified. The Jacobian of the lens equation is a matrix of the partial derivative of every variable in the lens equation. Since the single lens Equation (2.1.1) is real and only contains two variables, the Jacobian is a 1×1 matrix and

$$\frac{1}{\det J} = \frac{1}{J} = \frac{1}{du/dy_{\pm}}. \quad (2.1.4)$$

Then the adjustment for the single lens is simply to multiply by an extra factor of y_{\pm}/u , so that

$$A_{\pm} = \left(\frac{1}{\det J} \right) \left(\frac{y_{\pm}}{u} \right), \quad (2.1.5)$$

and the particular

$$A_{\pm} = \frac{1}{1 + \frac{1}{y_{\pm}^2}} \left(\frac{y_{\pm}}{u} \right). \quad (2.1.6)$$

The observed magnification is the addition of the magnification of each image. Inserting y_{\pm} from Equation (2.1.3) and summing the two magnifications will give the observed magnification of the event,

$$A_{\text{obs}} = A_{+} + A_{-}. \quad (2.1.7)$$

2.1.2 Single Lens Light Curve

The light curve has one peak because the system includes one lens. The impact parameter μ_0 determines the initial separation of the star and lens, and or affects the shape of the curve. Below are two examples. First, with an impact parameter of $\mu_0 = 0$ where the star passes directly behind the lens and exhibits a moment where the magnification is infinite. Then, the curve is shown with an impact parameter varying from $\mu_0 = 0.2$ to $\mu = 2$ when the magnification levels out to 1.

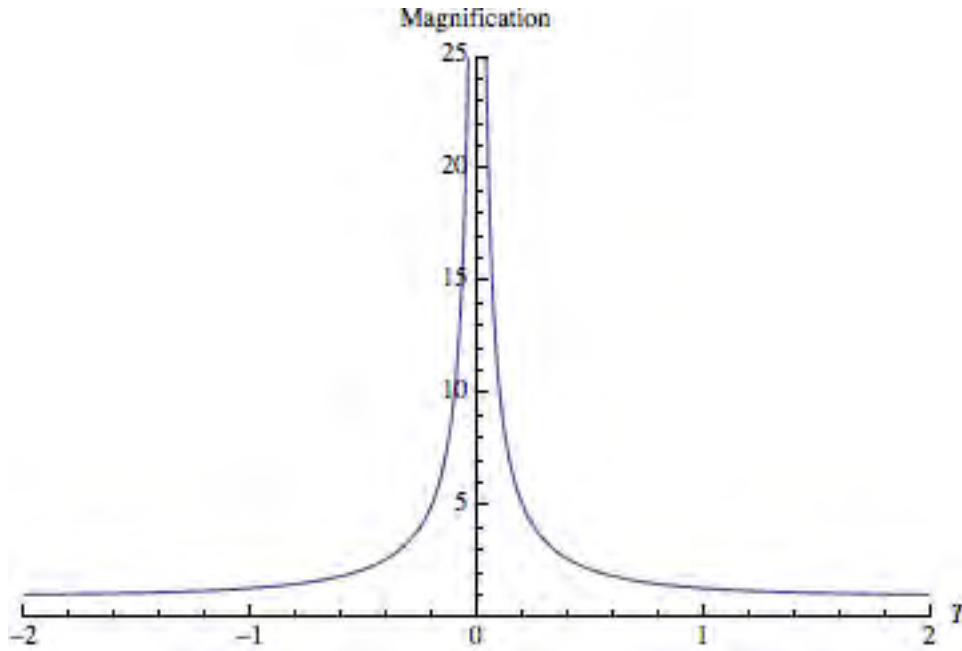


Figure 2.1.1: This is a magnification vs. time graph for a single lens with an impact parameter of $\mu_0 = 0$. This model is based on the unrealistic assumption of a point star and therefore shows infinite magnification.

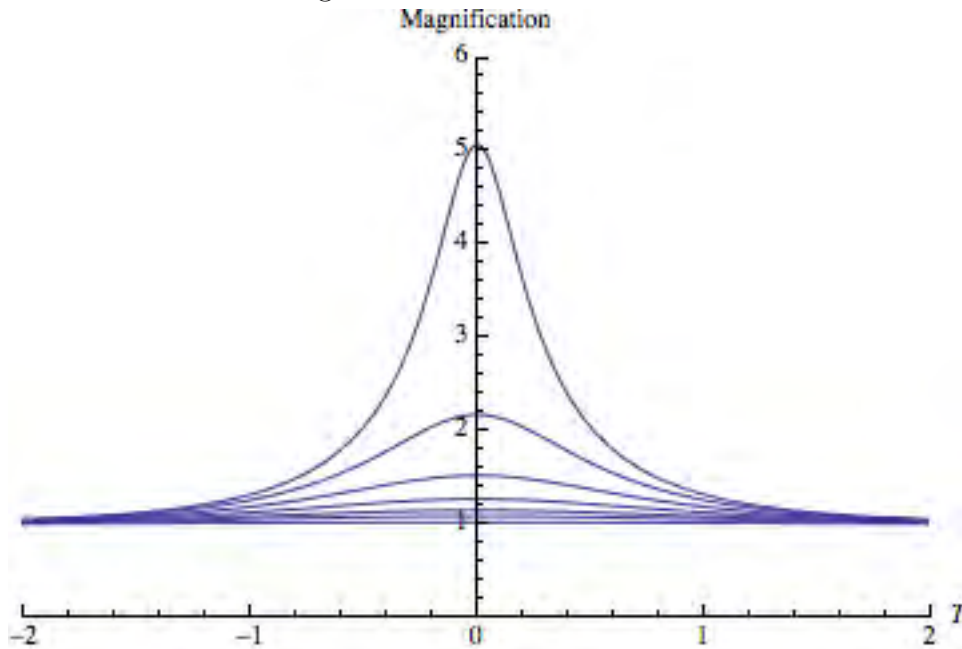


Figure 2.1.2: This is a magnification vs. time graph for a single lens with varied impact parameter. The tallest peak has an impact parameter of $\mu_0 = 0.2$, and then it increases incrementally in steps of 0.3 until reaching the value of $\mu_0 = 2$. Once the impact parameter reaches $\mu_0 = 2$, the curves flatten to a constant value of 1.

2.1.3 Single Lens with a Finite Star Size

The simplest route to convert from a point-like star approximation to a more realistic finite star is to assume the star is spherical with uniform brightness. Following a method by Witt and Mao [?witt1990minimum], I have approximated the star to be a circle situated in the complex plane with radius r and position ζ_0 ,

$$\zeta = \zeta_0 + re^{i\phi}. \quad (2.1.8)$$

Here ζ_0 is assumed to be on the real axis. The total area of this star can be found by integrating as ϕ rotates from 0 to 2π . This is simple since the total area of a circle with radius r is equal to πr^2 .

Finding the total magnification with a finite source is similar to the point star approximation used in Section 2.1.1. The total magnification can be found by taking the ratio of the total area of the images to the total area of the star.

Finding the area of both images requires a bit more work. To begin, I solve the single lens Equation (2.1.1) for image positions $z_{1,2}$. Equation (2.1.3) can be algebraically rearranged to the more convenient form of

$$z_{1,2} = \frac{\zeta}{2} \left(1 \pm \sqrt{1 + \frac{4}{\zeta^2}} \right). \quad (2.1.9)$$

Substituting ζ from Equation (2.1.8) provides

$$z_{1,2} = \frac{\zeta_0 + re^{i\phi}}{2} \left(1 \pm \sqrt{1 + \frac{4}{\zeta_0^2 + 2r\zeta_0 \cos \phi + r^2}} \right), \quad (2.1.10)$$

when $0 \leq \phi \leq 2\pi$.

Euler's Formula states that

$$e^{i\phi} = \cos \phi + i \sin \phi, \quad (2.1.11)$$

and can be used to separate Equation (2.1.10) into its real and imaginary parts. I define the real part as

$$x(\phi) = \frac{\zeta_0 + r \cos \phi}{2} f_{1,2}(\phi), \quad (2.1.12)$$

and the imaginary part as

$$y(\phi) = \frac{r \sin \phi}{2} f_{1,2}(\phi). \quad (2.1.13)$$

For clarity it is convenient to define a function for the last part of Equation (2.1.10)

$$f_{1,2}(\phi) = \left(1 \pm \sqrt{1 + \frac{4}{\zeta_0^2 + 2r\zeta_0 \cos \phi + r^2}} \right). \quad (2.1.14)$$

The area of this image with total area D and boundary γ would take the form

$$\text{Area} = \int_D dy \hat{y} \times dx \hat{x}. \quad (2.1.15)$$

This integral can be simplified from an area integral to a line integral. First, I define the coordinate system so the image is symmetrical over the diagonal axis. In order to use this method it must be assumed that the image can be positioned this way.

The argument of the integral can be rearranged by realizing that

$$(dy \hat{y} \times dx \hat{x}) \text{ is equivalent to } (-dx \hat{x} \times dy \hat{y}). \quad (2.1.16)$$

Because we are situated in parity symmetry, flipping the cross product or flipping the axes is known as a parity transformation and gives an equivalent result with only a sign change. Equation (2.1.15) can be expanded as

$$\frac{1}{2} \int_D (dy \hat{y} \times dx \hat{x} - dx \hat{x} \times dy \hat{y}). \quad (2.1.17)$$

This new version is convenient because Stokes's Theorem can be used to convert the surface integral of the cross product to a line integrals around the boundary γ . Equation (2.1.17) simplifies to

$$\frac{1}{2} \int_{\gamma} [(ydx) - (xdy)]. \quad (2.1.18)$$

Another parity transformation can be used to change the argument of the second integral from xdy to $-ydx$ finally yielding

$$\frac{1}{2} \int_{\gamma} [ydx - (-ydx)] = \int_{\gamma} (ydx). \quad (2.1.19)$$

The magnification can be found by taking the ratio of the Equation (2.1.19), to the total area of the star, πr^2 . The total magnification of each image becomes

$$A_{1,2} = \frac{1}{\pi r^2} \int_0^{2\pi} y(\phi) \frac{dx(\phi)}{d\phi} d\phi. \quad (2.1.20)$$

I used Mathematica to solve this integral as shown in Appendix .2. By summing the two magnifications, I was able to create a light curve for a specified radius and impact parameter.

The following page displays figures for a star with radius $r = 0.1$. As radius increases the curve becomes wider with lower magnification. The first graph shows $\mu_0 = 0$ with the notable feature that we no longer see infinite magnification for any location. Comparing the light curve of a hypothetical point star, Figure 2.1.1, to this more realistic light curve for a finite star will illuminate the limitations of assuming a point source. Figure 2.1.3 can be compared with the analogous point star curve though it should be noted that the range of the two Figures is different. While increasing the impact parameter, the finite source curve approaches magnification of 1 slightly faster. When interpreting an actual microlensing event, star and lens would be more closely aligned than the point star model would indicate.

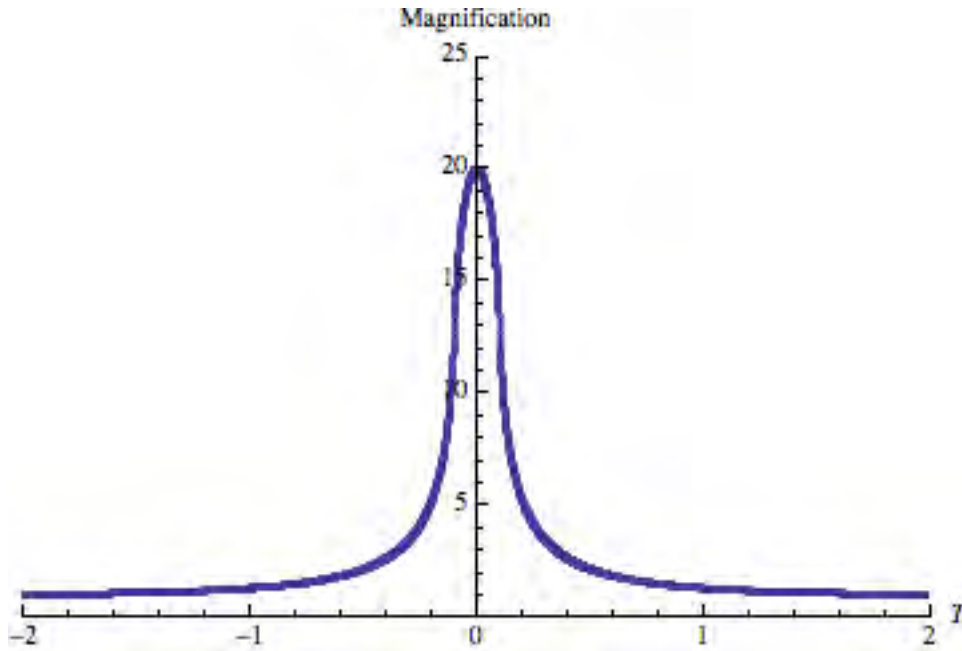


Figure 2.1.3: A magnification vs. time graph for a single finite lens with a radius of $r = 0.1$. Here the impact parameter is $\mu_0 = 0$ and shows a peak magnification near 20.

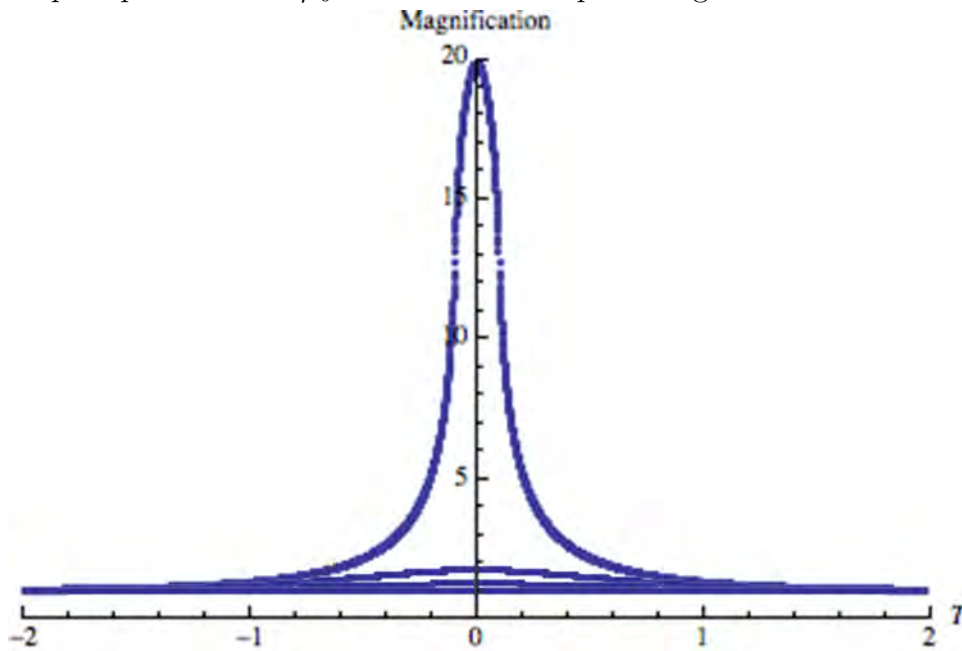


Figure 2.1.4: A magnification vs. time graph for a single finite lens with varied impact parameter. The tallest peak has an impact parameter of $\mu_0 = 0.2$, which increases incrementally in steps of 0.45 until reaching the value of $\mu_0 = 2$. Once the impact parameter reaches $\mu_0 = 2$, the magnification curve has flattened to a constant value of 1.

2.2 Double Lens

2.2.1 Double Lens Magnification from the Summation of Image Magnifications

For two lenses, I begin with Equation (1.3.8) where $N_L = 2$ and

$$\zeta = z - \left(\frac{m_1}{\bar{z} - \bar{z}_1} + \frac{m_2}{\bar{z}_2 - \bar{z}} \right). \quad (2.2.1)$$

By placing both lenses on the real axis and then centering the real axis so its origin is directly between the two lenses, it is possible to represent both positions with one number [1] where

$$z_1 = -z_2. \quad (2.2.2)$$

Then by defining the real axis as the line between the lenses,

$$z_1 = \bar{z}_1. \quad (2.2.3)$$

I adjust the representation of mass in accordance with convention and to make the algebra cleaner. Instead of representing the masses as m_1 and m_2 , I use the average of the masses,

$$m = \frac{(m_1 + m_2)}{2}, \quad (2.2.4)$$

and half of their difference (distance from the average),

$$\Delta m = \frac{(m_2 - m_1)}{2}. \quad (2.2.5)$$

The lens equation becomes

$$\zeta = z + \left(\frac{m - \Delta m}{\bar{z} - z_1} + \frac{m + \Delta m}{-z_1 - \bar{z}} \right). \quad (2.2.6)$$

Following an article by Hans J Witt and Shude Mao, [1], I take the conjugate of Equation (2.2.6), solve for \bar{z} , then substitute that back into Equation (2.2.6). Clearing the denominator results in the lens equation reorganized as the 5th order polynomial in z of

$$G_1(z) = \sum_{j=0}^5 (c_j)(z^j). \quad (2.2.7)$$

The coefficients of this equation are listed explicitly in the article by Hans J Witt and Shude Mao [1]. I could not numerically solve for the roots of the equation and create a light curve if my equation contained any symbolic coefficients. The same article by Witt and Mao convinced me the resultant method would be better suited for my goal.

2.2.2 Double Lens Total Magnification using Resultant Method

I began this technique with the 5th order polynomial of Equation (2.2.7) already known. Following an algebraic technique detailed in this same article, I obtained an 8th order polynomial in z . The previously used equation for magnification Equation (1.4.1) where

$$A_j = \frac{1}{\det J} \Big|_{z=z_j}, \quad (2.2.8)$$

can be rearranged to the form

$$A_j \left(1 - \frac{\partial \zeta}{\partial \bar{z}} \frac{\partial \bar{\zeta}}{\partial \bar{z}} \right) = 0, \quad (2.2.9)$$

where

$$\frac{\partial \zeta}{\partial \bar{z}} = \frac{m - \Delta m}{(\bar{z}_1 - \bar{z})^2} + \frac{m + \Delta m}{(-\bar{z}_1 - \bar{z})^2}. \quad (2.2.10)$$

In order to eliminate \bar{z} , I took the conjugate of Equation (1.3.8) and found

$$\bar{z} = \bar{\zeta} - \frac{m - \Delta m}{(\bar{z}_1 - \bar{z})^2} + \frac{m + \Delta m}{(-\bar{z}_1 - \bar{z})^2}. \quad (2.2.11)$$

I used this to replace \bar{z} in Equation (2.2.10), and was left with a polynomial in z of order 8 in the form

$$G_2(z) = \sum_{j=0}^8 (b_j)(z^j). \quad (2.2.12)$$

Taking the resultant of these two polynomials eliminates the dependence on z and I am left with a polynomial relating star position and magnification. The resulting polynomial is exceedingly large and can be found in Appendix .3. The magnifications can be summed to find the total or observed magnification. The resulting light curves are shown and interpreted in Section 2.2.3

2.2.3 Double Lens Light Curves

For two lenses located in close proximity, the caustics appear as a diamond like curve. Caustics are the star positions (in the star plane) where the images merge. This is observed as a peak of infinite brightness on the light curve of the star. It will be useful to consult the caustic shown in Figure 2.2.3 to interpret Figures 2.2.3 and 2.2.2.

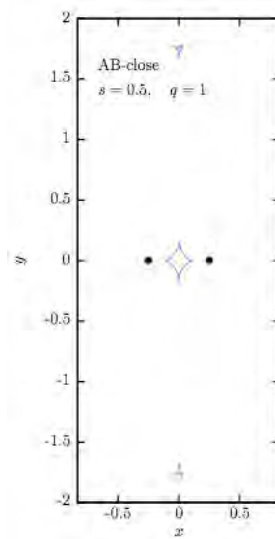


Figure 2.2.1: The pink line connects the caustics for a system of two point lenses. The lenses are represented by small black dots located at $x = \pm 0.25, y = 0$. This image was originally printed in an article by Luhn, Penny and Gaudi [22].

For the two lens case if the star is inside the caustic, five images are created, and if the star is outside of the caustic three images will be created. In both cases there will be five solutions to the lens equation. When the star is outside of the caustic two of these solutions are spurious. The spurious solutions do not correspond to actual image positions and must be discarded. More information on this topic can be found in a detailed study by Schneider and Weiss [5].

I have depicted models where the star is inside the caustic curve and all five images are valid. The star is within the caustic under the condition $z_1^2 < 2m$ where z_1

and m are defined by Equations (2.2.2) and (2.2.4). The two lenses have equal mass in all of my models.

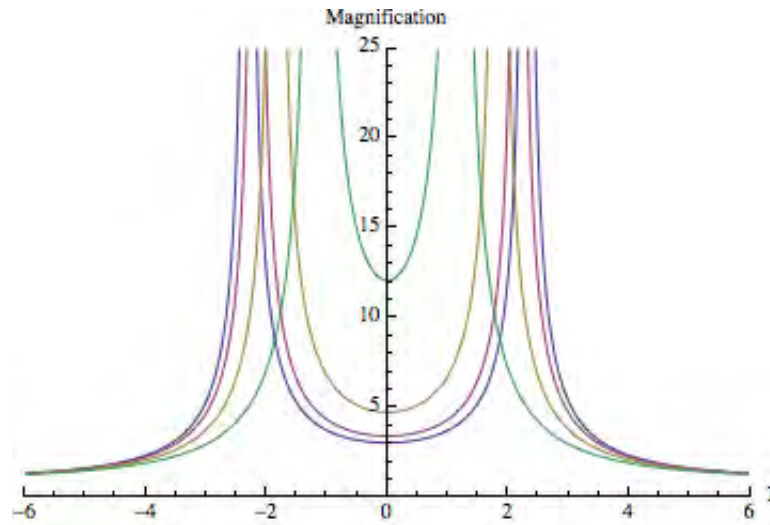


Figure 2.2.2: This is a magnification vs. time graph for two gravitational lenses as the impact parameter increases from $\mu_0 = 0.2$ to $\mu_0 = 2$ in increments of 0.6. The lenses are located at $z_{1,2} = \pm 3$ and their masses are $m_{1,2} = 10$. When μ_0 is near zero, the star crosses the caustic along the line $y = 0$ in Figure 2.2.3. As μ_0 increases, the star crosses the caustic at increasing distances from the y -axis in Figure 2.2.3.

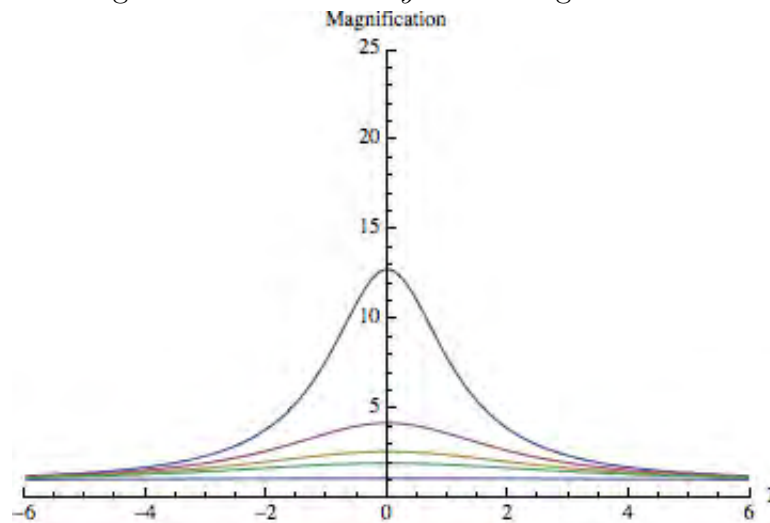


Figure 2.2.3: This is a magnification vs. time graph for two gravitational lenses as the impact parameter increases from $\mu_0 = 2$ to $\mu_0 = 5$ in increments of 0.6. The lenses are located at $z_{1,2} = \pm 3$ and their masses are $m_{1,2} = 10$. Near $\mu_0 = 2$ the two peaks merge into one. At this point, the star is crossing the caustic (in Figure 2.2.3) near a cusp. As μ_0 continues to increase, the star's path shifts away from the caustic and the light curve levels out to a magnification of 1 when $\mu_0 = 5$.

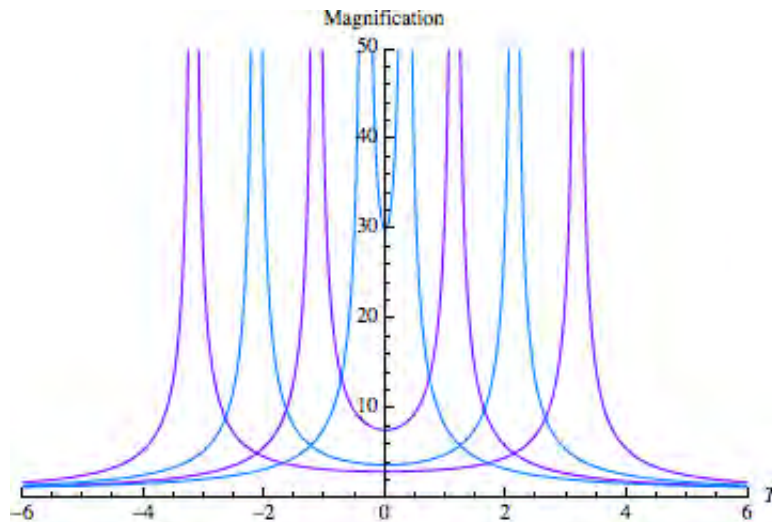


Figure 2.2.4: This is a magnification vs. time graph for two gravitational lenses as the distance between the lenses is varied from $z_{1,2} = \pm 1$ to $z_{1,2} = \pm 4$ in integer increments. The impact parameter is held constant at $\mu_0 = 0.2$ and the masses are equal at $m_{1,2} = 15$.

The code I used to create these models can be found in Appendix .3 or at bohr.physics.berkeley.edu/hal/projects/eturrell.

2.3 Triple Lens

2.3.1 Triple Lens Total Magnification using Resultant Method

The triple lens proceeds in a similar fashion as the double lens. For two lenses I manipulated the lens equation to find one 8th order polynomial and one 5th. For three lenses I will work with one 10th order polynomial and one of order 13. For three lenses, I begin with Equation (1.3.8) where $N_L = 3$ to find

$$\zeta = z - \left(\frac{m_1}{\bar{z} - \bar{z}_1} + \frac{m_2}{\bar{z} - \bar{z}_2} + \frac{m_3}{\bar{z} - \bar{z}_3} \right). \quad (2.3.1)$$

The 10th order polynomial in z is given in a paper by Sun Hong Rhie [24]. He writes the polynomial in the condensed form

$$0 = \sum_{k=1}^{10} \text{cff}(k) z^k, \quad (2.3.2)$$

where $\text{cff}(k)$ is a function that calls coefficients H_{ij} which are themselves polynomials indexed in a 4×10 matrix. It was immediately obvious that this polynomial could not function as written. The sum does not include a 0th order term, which means it would create a 9th order polynomial and could not be an accurate manipulation of the three lens equation. In his paper, Rhie summarizes intermediate steps he took before landing at the final form of this polynomial. I recreated an earlier form of this polynomial and realized that there was, at some point, a 0th order term. After creating the polynomial, I realized that his condensed form would function if it were defined as

$$R_1(z) = \sum_{k=1}^{10} \text{cff}(k) z^{k-1}. \quad (2.3.3)$$

Also, a column of zero's would need to be added to the matrix H . With these adjustments, I was able to recreate his polynomial. The polynomial is again exceedingly large and can be found by the Mathematica file in Appendix .4.

To eliminate the dependence on z using the resultant, I needed to create one more polynomial in z . For two lenses Mathematica was able to handle a messy polynomial, but three lenses proved to be too algebraically rigorous. In order to sort out the polynomial I ended up clearing the denominator and taking a Power Series expansion around $z = 0$ to collect the coefficients. The resulting polynomial is many many pages long, too long to be included in my Appendix file, but takes the form

$$R_2(z) = \sum_{j=0}^{13} (d_j)(z^j). \quad (2.3.4)$$

Contrary to the two lens case, Mathematica was not able to take the resultant of the two polynomials if they contained any unspecified variables. I do not have a reason to leave any of the variables unspecified, but have not continued at this point. Also the conjugate function causes unpredictable problems when interpreting these polynomials. Complex variables are required to describe the image positions for three lenses, so this

obstacle has been difficult to circumvent. We have been able to find solutions with specified coefficients.

2.4 Future Goals

In the finite lens case, we encountered a related situation. We were required to specify every variable before completing a numerical integration. As a solution, we specified every variable and iterated over gradually increasing values of T , reevaluating the function and producing one point on the graph for each specified T . We created a light curve as a scatterplot of these points. I am currently considering a method along the same logic to be applied for the three lens resultant method.

I was originally drawn to modeling light curves after reading a paper by Jacob Luhn [22] where he promoted microlensing as a technique to discover three body systems. In the future I would like to create a functioning light curve for a three lens system. Then, I would turn toward making models that reflect more realistic situations. I plan to explore whether the resultant method could accommodate a finite source. I would hopefully be able to expanded the finite star model to two and three lens systems.

3

Radio Interferometry

This chapter embarks on the expected but major shift in my project. From here forward, I explore radio astronomy through designing and constructing a radio interferometer. With the goal of measuring the diameter of the Sun, I hope to exhibit why a radio interferometer is an interesting and appropriate model for the task, and then describe how to build something akin to mine. First, I will place my project in history by giving credit to inventions that preceded and informed my interferometer. Reflecting on the advantages and disadvantages of similar technology will also justify my design and construction.

Scientific progress does not trudge steadily along a predetermined path toward ideal efficiency, guided by the principles of the universe and mathematical truths. I hope to highlight how the direction of scientific inquiry is related to the society it serves. I will explore various influences that steered the development of radio technology in Section 3.1 including political goals and the availability of funding during WWII, then the space age and availability of materials. In Section 3.2 and Section 3.3, I will delineate my building process, flush with tips oriented toward an amateur radio astronomer completing a similar project.

3.1 Overview of Radio Interferometry

In my introduction I discussed the detection of the first extraterrestrial radio discovery that occurred in 1930 when Karl Jansky identified radio noise originating from the Milky Way. Long before this was possible, scientists began developing radio technology with the goal of communicating over longer earth bound distances. In 1901, Guglielmo Marconi developed the first antenna system to complete transatlantic communication.

An antenna consists of conducting elements connected to a radio transmitter or receiver. During operation, a transmitter forces an oscillating stream of electrons through the antenna. The electrons create a magnetic field around the antenna and an electric field along the antenna. This electromagnetic field propagates as a transverse wave emanating in all directions away from the antenna. The rate at which the transmitter sends electrons through the wire directly controls the frequency of the emitted waves. The antenna can also function as a receiver. In this mode, oscillating electromagnetic waves exert a force on electrons in the antenna. The electrons in the antenna oscillate and send this signal toward the receiver. The receiver amplifies the signal emanating from the antenna.

While designing his antenna to transmit signal over increasing distances, Marconi realized that the effective area of the antenna, as well as its gain, were important features of an antenna system [13]. Gain is typically a measure of an antenna's quality as a transmitter and its effective area measures an antenna's efficiency as a receiver. Since any antenna can act as a transmitter or receiver, these two measurements of efficiency are closely related. The Lorentz reciprocity theorem of electrodynamics describes precisely how gain and effective area are two ways to describe the same features of an antenna. Depending on how an antenna is intended to function, one or the other would be more useful.

Ideally, an antenna can transmit signal with intensity distributed equally over all radial directions. If this were achieved, the signal could be relayed between two antenna

in any alignment. In reality, an antenna has an orientation and the signal is directionally dependent, which is also described by an antenna's gain. A high gain antenna radiates most of its power in one direction, while a low gain antenna distributes the intensity of the signal over a wider angular area. The gain of an antenna is determined by

$$G = 10 \log \frac{I}{I_{\text{iso}}}, \quad (3.1.1)$$

where I is the intensity of the signal in the direction of maximum output and I_{iso} would be the intensity of the signal if the total intensity were distributed equally in all radial directions, that is, isotropically.

In receiving, the effective area of an antenna describes the percentage of the power of a passing electromagnetic wave an antenna can translate to the receiver. The effective area of an antenna, a measurement of efficiency, can be determined by

$$A_{\text{eff}} = \frac{\lambda^2}{4\pi} G = \frac{(c/f)^2}{4\pi} G, \quad (3.1.2)$$

for a specified wavelength λ or frequency f where c is the speed of light and G is the gain of the transmitter.

To increase the efficiency of his antenna systems, Marconi increased the size of each antenna and suspended them higher into the sky. In Cornwall, Marconi suspended an antenna by an unsteady wooden post. In Newfoundland, Marconi attached an antenna to a kite and flew the kite on a wire over 550 feet long. In 1901, Marconi's antenna in Newfoundland received three short clicks from Cornwall as the first wireless signal was transmitted across the Atlantic.

Over the years, many improvements on Marconi's fundamental system were made. Many antennae can be combined in a phased array, called an aperture array, to function as a more powerful system. The transmitter or receiver accounts for the phase difference between each element so the system effectively functions as one large antenna.

Array systems were extremely influential during WWII. The flat profile of an aperture array is much easier to “seamlessly incorporate into the surface structure of other systems, for example, vehicles, ships, aircraft fuselage and missile skins” [13]. Military equipment often needs to be flexible and portable. Array systems can be easily disabled, transported and reassembled and are generally light weight. However, complex cabling of aperture arrays was also known to be large and temperamental with electrical problems that were difficult to diagnose and locate [13].

In the 1960’s, the parabolic dish largely replaced array systems in radio technology. A parabolic dish reflects the radio energy of the source onto a small antenna located at the focus of the dish. The strength of a radio source is determined by the amount of energy per second per unit frequency interval on a unit area of the telescope, called the spectral flux density, $S(f)$ [9]. To determine the power collected by the receiver, the spectral flux is integrated over the collecting area of the telescope, a , and the frequency interval the antenna is sensitive to, known as the bandwidth. Using Equation (3.1.2) where A_{eff} specifies the efficiency of the antenna for a frequency f , the power can be determined by

$$P = \int_a \int_f S(f) A_{\text{eff}} df da. \quad (3.1.3)$$

The shift toward the parabolic dish occurred as reliable methods of wireless communication surpassed radio, wartime funding waned, and radio technology turned its focus toward astronomy. The parabolic dish arrangement is in many ways better suited for radio astronomy. A parabolic dish allows for radio transmission at much higher frequencies and “aided the astronomer’s task of cross-matching radio sources with higher resolution optical catalogues” [13]. Scientists hoped to map out the Milky Way and other Galaxies using the spectral line associated with neutral hydrogen, which emits at the high frequency of 1.4 GHz. A steel dish offers greater stability and reliability, and the centrally located antenna could be highly specialized and temperature controlled.

A parabolic dish reflects the radio energy of the source onto a small antenna located at the focus of the dish. The strength of a radio source is determined by the amount of energy per second per unit frequency interval on a unit area of the telescope, called the spectral flux density, $S(\nu)$ [9].

Increasing the area of the collecting surface increases the power of the signal collected. An interferometer is capable of simulating a much larger parabolic dish by deflecting signal onto the parabolic dish from areas beyond of the range of the dish. My interferometer uses the method of interferometry developed by Michelson and Morley and popularized by experiments such as LIGO. My interferometer is closely aligned to the design developed by Jin Koda et. al. [4]. It consists of four mirrors that deflect toward a 1-meter parabolic dish. The collection area of a single dish is only $\frac{\pi r^2}{4}$ meters² $\approx .78$ meters². The interferometer setup increases the collection area to ≈ 1.89 meters². A detailed sketch of my interferometer design is shown on the following page.

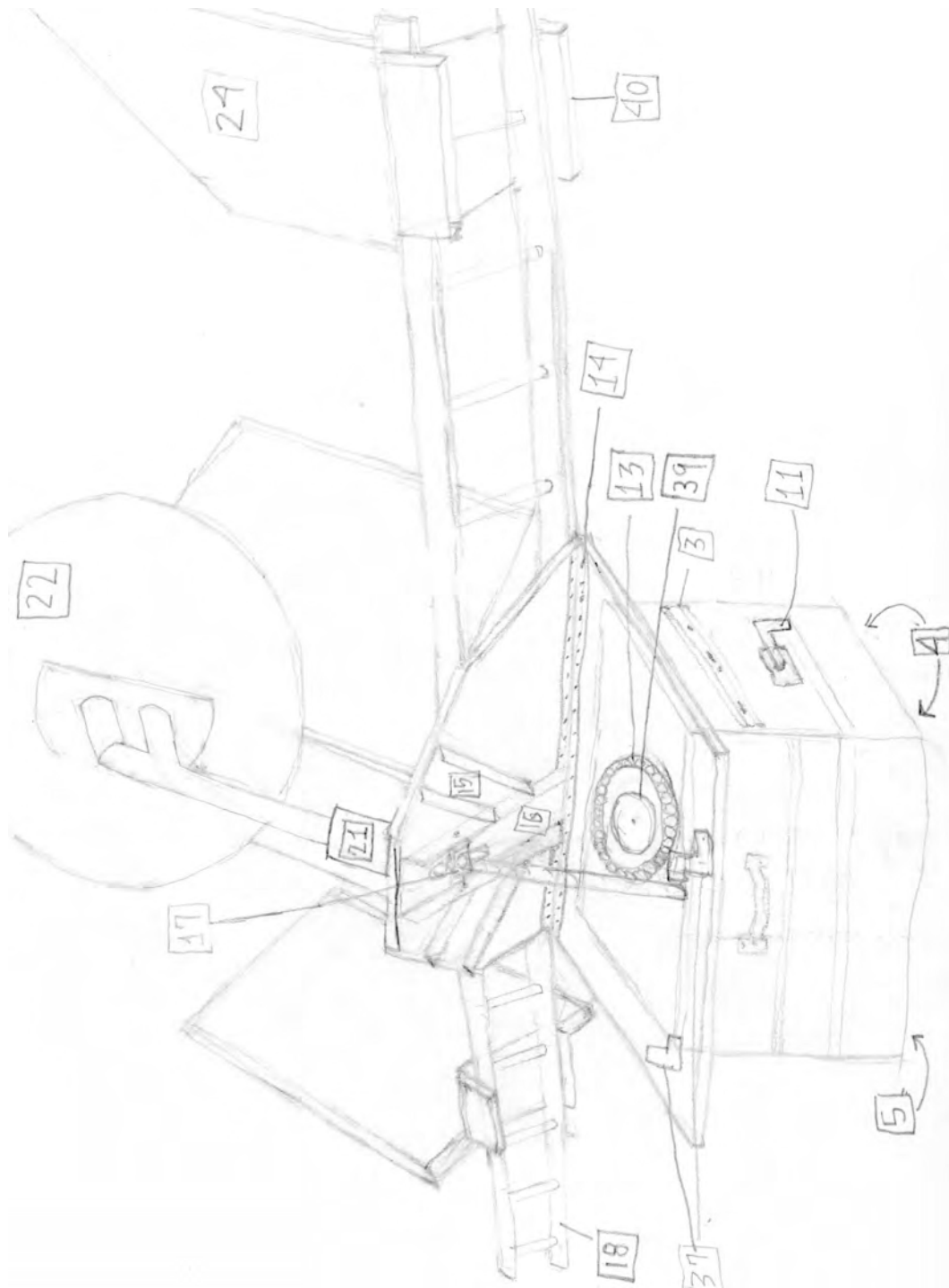


Figure 3.1.1: A detailed sketch of my interferometer design. The parts are labeled and will be referred to repeatedly throughout the chapter. I have spent considerable time developing a more rigorous three-dimensional model of my system using the program Inventor Professional. I haven't included these in progress sketches, but could make them available to anyone interested.

3.2 Interferometer Construction

3.2.1 Materials List

Label	Item	Part Number	Manufacturer	Quantity	Unit Price	Price
1	Three sheets of 1/2" plywood, various 2x4, 2x2, Screws and Glue		Home Depot	1	~\$200	\$200.00
2	YTZ7S Scorpion 12v Motorcycle Battery	YTZ7S	BatteryStuff.com	1	\$44.95	\$44.94
3	24" steel drawers slides	11965A127	McMaster-Carr	1	\$24.70	\$24.70
4	Swivel caster wheels	4941T13	McMaster-Carr	2	\$39.32	\$78.64
5	Rigid caster wheels	4941T15	McMaster-Carr	2	\$37.20	\$74.40
6	1/2" x 3ft steel rod	89905K11	McMaster-Carr	3	\$7.16	\$12.48
7	2" sleeve bearing block	4178K2	McMaster-Carr	1	\$36.36	\$36.36
8	1" sleeve bearing block	4178K12	McMaster-Carr	6	\$30.00	\$180.00
9	1/8" x 1" x 3ft flat stock steel	9516K47	McMaster-Carr	4	\$22.80	\$91.20
10	3ft 5/8" - 11 fully threaded steel rod	90322A330	McMaster-Carr	1	\$13.43	\$13.43
11	Crank handle	6129K6	McMaster-Carr	1	\$29.20	\$29.20
12	1" x 1" x 2' steel bar	9143K21	McMaster-Carr	1	\$26.27	\$26.27
13	10 1" steel ball bearings	96455K62	McMaster-Carr	7	\$6.22	\$43.54
14	Steel piano hinge	1569A962	McMaster-Carr	1	\$26.67	\$26.67
15	3" x 3/2" x 3 ft aluminum U-channel	1630T31	McMaster-Carr	1	\$24.65	\$24.65
16	4" x 2" x 3ft aluminum U-channel	1630T33	McMaster-Carr	1	\$35.53	\$35.53
18	16 ft fiberglass manhole ladder	G0793186	Zoro	1	\$247.53	\$247.53
19	metal brackets	17715A44	McMaster-Carr	2	\$2.00	\$4.00
20	1/2" x 6" x 6" aluminum plate	9246K493	McMaster-Carr	1	\$15.80	\$15.80
21	3" x 3" x 6" aluminum block	9008K62	McMaster-Carr	1	\$36.04	\$36.04
22	1 - meter Satellite Dish with AZ/EL Pole Mount	DS-3100	Solid Signal	1	\$89.95	\$89.95
24	2ft x 3ft sheet aluminum		Home Depot	4	\$25.00	\$100.00
					Total Price	\$1,435.33

Figure 3.2.1: The materials I used to construct my radio interferometer including part number and manufacturer. The numbers in the left hand column will be used in the image and throughout the chapter when referencing a part.

3.2.2 Methods

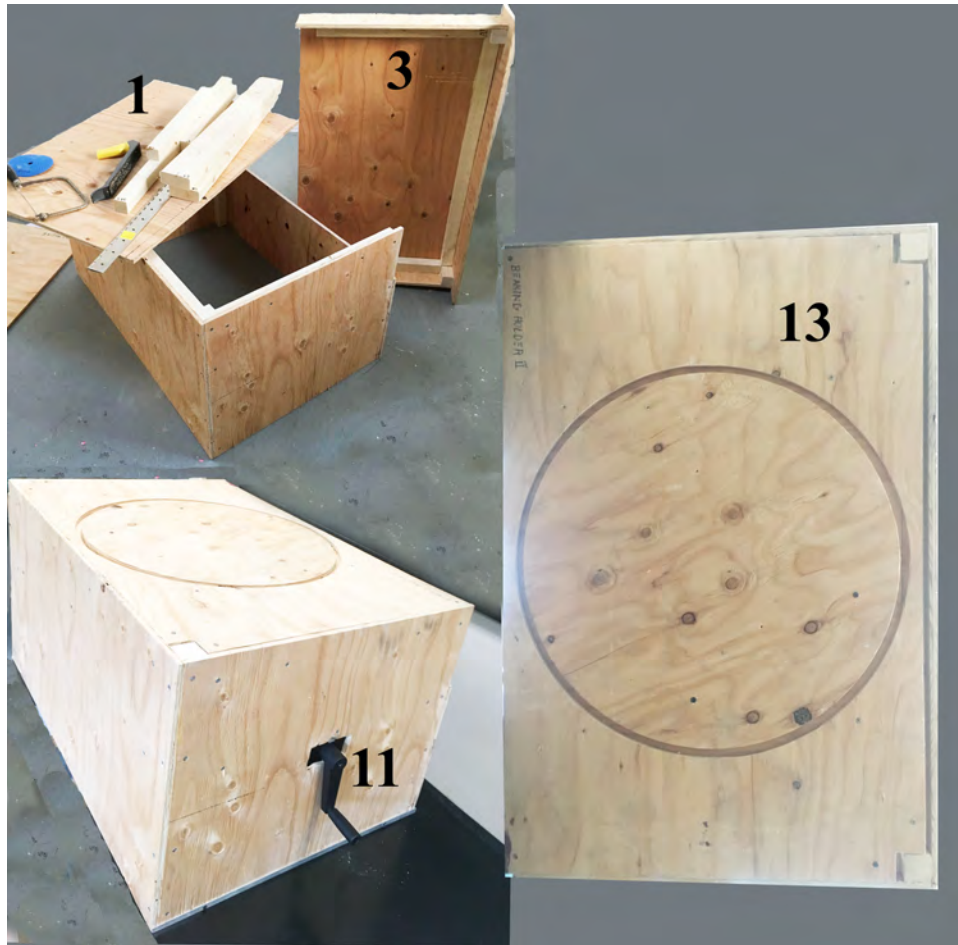


Figure 3.2.2: These photographs show the wooden base structure. The drawer is shown in the upper left photo, and the crank handle protruding out of the box is shown in the bottom left photo. The ball bearings ride along the track shown here.

The box structure was constructed using plywood and pine studs fastened with carpenters wood glue and screws [1]. The size of the box was determined by the width of the storage facility. Most importantly, the wood structure should be low and wide enough to stabilize the parabolic dish and mirrors system. The upper half of the box is a drawer sized 4in x 21in x 35in and is shown in Fig. 3.2.2. This drawer will be used to store the aluminum electronics box and 12 Volt battery [2] during observational runs. This drawer would be able to carry weights for added stability if observing under windy conditions. With this in mind, I chose 24" steel drawer slides [3] for durability. Special

detail should be paid to installation of drawer slides, as they require precision and have very little room for error with my current design.



Figure 3.2.3: These photographs depict the wheels and wheel deployment system. The structure shown in the upper right photo fits inside of the box in the area shown in the lower left photo. I am chiseling a hole for the crank handle in the upper left photo. In the bottom left photo, my sister Cora is welding a support structure in a configuration to maximize strength.

The bottom section of the box structure contains the wheel system. Due to the total weight of the structure, wheels are necessary to move from storage to observation location. The best zone for observation may be an open field free from tree coverage or the top of a hill. In order to reach these locations I choose two swivel air-ride casters [4] for the front and two rigid air-ride casters [5] for the back that are capable of traversing rugged terrain while absorbing shock to protect the equipment. Shock absorbent wheels are necessary for moving the equipment but are undesirably unsteady while collecting

data. To combat this, I have designed a wheel deployment system that will elevate the box during transfer then lower the operator to rest firmly on the ground for data collection. The wheel structure is controlled by a 1.5" screw [10] mounted onto a crank [11] extruding from one side of the box. The other end of the screw is threaded into a square steel bar [12] inside of the box. Shifting the steel bar along the screw and horizontally to the ground initiates a lever system (using parts [6] [7] [8] and [9]) to simultaneously separate a frame connecting all four wheels (see Figure 3.2.2) away from the main structure of the box. The wheels structure seems complicated but functions similar to a wheel jack. With only a few rotations of the crank handle, the wheels can be lowered an inch below the bottom edge of the box, adequate for moving the box over pavement or grassy terrain.

Flush with the top of the box are two pieces of plywood supported around their perimeter. A 22" diameter circle with 3/4" depth and 3/4" width is routed into the top piece of plywood as shown in Figure 3.2.2. This circle will hold ball bearings to allow for smooth horizontal movement of everything above this point. Precision of the circle is necessary, and sharp corners of the track help to reduce friction with the ball bearings. To achieve this, I used a CNC router to cut two our circles through the top piece of plywood. I then removed the rim of wood between the two circles and mounted the remaining wood onto another piece of plywood. With use, this double thick plywood support appears to bend under the weight of the interferometer. Added support, potentially in the form of cross beams underneath the plywood, is recommended for an improved design.

Riding in this track are sixty-nine one inch steel ball bearings [13]. I chose steel for cost efficiency, and recommend a much lighter but more expensive plastic ball bearing if possible. On the reverse side of the ball bearing track is the two-piece contraption pictured in progress in Figure 3.2.2. These two pieces will have most of the interferometer parts mounted on them including the motors, parabolic dish, and ladder. This photo shows the initial steps in preparing these pieces for the load they will bear. The underside of the

rectangular half has a routed groove to receive the ball bearings. This groove is again 22" diameter circle but here only 1/4" depth and 1/2" width. I used the same procedure as for the first side's circle but used only single thickness plywood here. The hinge [14] proved to be difficult to mount using bolts while trying to preserve maximum angular movement of the two pieces. This hinge will undergo substantial strain so its security should be carefully planned. In the end, I secured the hinge with 3/4" - 20 bolts facing outward.

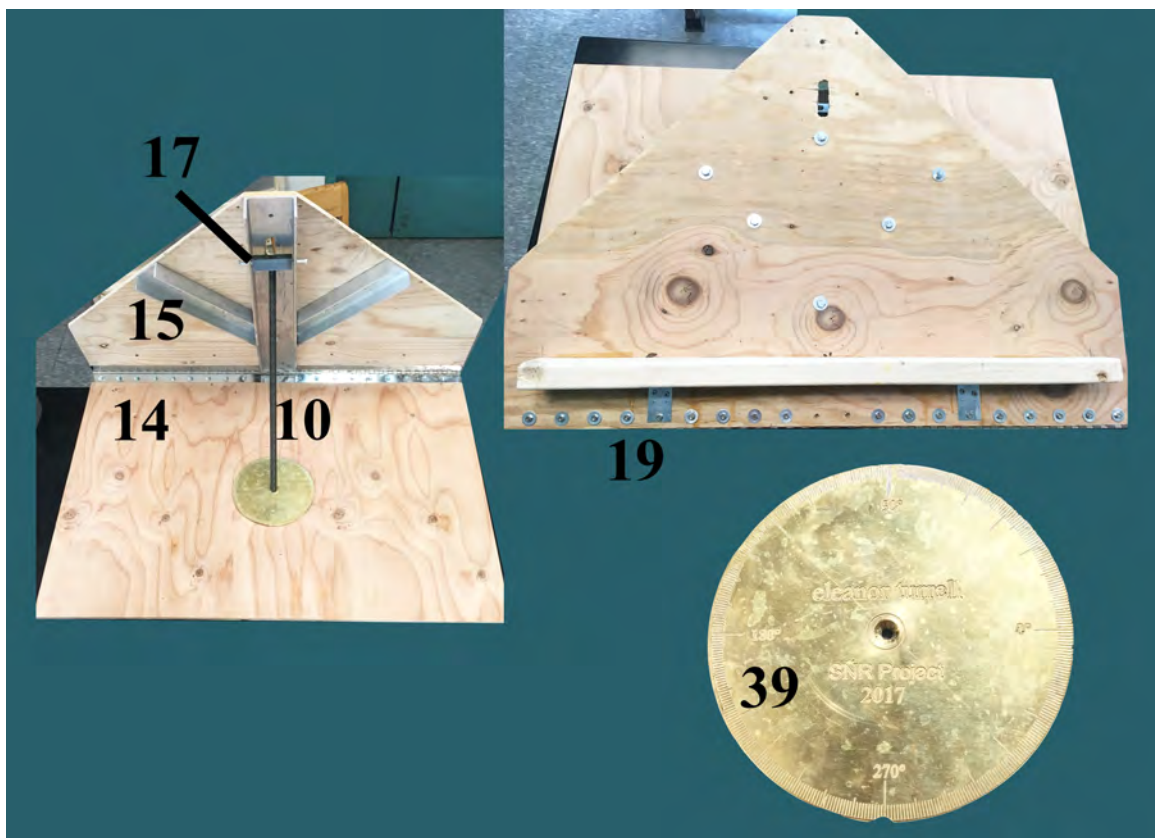


Figure 3.2.4: This photograph shows the mounting system that will be positioned on box pictured in Figure 3.2.2. Ball bearings support movement between the box and this structure. The antenna and ladder are mounted on the plane shown in the upper right photograph. The degree dish [39] was engraved to measure the rotation of the system. The 'airplane' support structure is also pictured.

Similar to the hinge, the top plank endures exceptional strain and should be reinforced. For this I have designed the 'airplane,' a structure of aluminum channels

mounted on the underside of the plank. An improved design might rotate the two wings of the airplane [15] to wedge against the supporting structure and distribute torque over a larger area.

The straight channel [16] holds a steel block [17] to support the motorized lift mechanism. The steel block is free to rotate in its position and tapped in the center. Above the steel block there should be a slot clear through both the wood and steel channel. As the motor turns the screw to lower the top plank, the screw will protrude out through this slot. Refer to Section 3.3 for more information about the motor system.

The top plank supports the data collection equipment. The ladder [18] rests on a wooden 2x4 along the bottom of the plank. This support should be reinforced with metal brackets [19]. Above the ladder is a mount machined from an aluminum plate [20] and aluminum block [21] to hold the satellite dish. A one-meter diameter parabolic dish [22] reflects the signal onto an antenna (one of the functions of [23]) that leads into an electronic box for adjustment and interpretation.



Figure 3.2.5: The mirrors are created from aluminum sheets and wooden frames similar to a stretcher bar for painting. The mirror mounts are also shown here. Notice the mount is designed to slide along the ladder.

The radio signal is deflected toward the parabolic dish by mirrors. In fact, they are 2x4 foot aluminum sheets [24]. I chose sheet aluminum for durability while any aluminum at least 0.03 mm thick including double ply aluminum foil would be adequate and cost effective. As seen in the diagram, two mirrors are positioned nearer the ends of the ladder and utilized to collect the signal, while two centrally located mirrors are deflecting the signal onto the parabolic dish.

To mount the mirrors, I constructed wooden supports that rest on the outside of the ladder with enough room to allow the supports to slide along the ladder. I mounted the four mirrors at forty-five degree angles facing the appropriate directions. Three of the mirrors can be secured in place along the ladder while one should remain free to slide.

3.3 Adjusting Radio Signal

3.3.1 Materials List

Label	Item	Part Number	Manufacturer	Quantity	Unit Price	Price
23	Low Noise Block Feedhorn	QPH-031	The Satellite Shop	1	\$49.99	\$49.99
25	LabQuest2 interface	LABQ2	Vernier Software & Technology	1	\$329.00	\$329.00
26	Logger Pro software for LabQuest2	LP	Vernier Software & Technology	1	\$249.00	\$249.00
27	Power Inserter	PDI-PI-1	Solid Signal	1	\$1.99	\$1.99
28	Differential voltage probe for LabQuest2	DVP-BTA	Vernier Software & Technology	1	\$39.00	\$39.00
29	5 Volt power inverter	BP5277-50-ND	Digi-Key	1	\$6.75	\$6.75
30	50 Ohm SMA Male to 75 F Male Adaptor	PE7075	Pasternack Enterprises	1	\$95.78	\$95.78
31	.5 to 2.5 GHz Amplifier	ZX60-2534M-S+	Mini-Circuits	1	\$64.95	\$64.95
32	Bandpass Filter	VBFZ-1400+	Mini-Circuits	1	\$39.95	\$39.95
33	Square-Law Detector	20760	Ebay	1	\$29.90	\$29.90
34	Aluminum Electronics Box	UNC 4-6-10 PLAIN-ND	Digi-Key	1	\$48.43	\$48.43
35	Integrated Circuit	CA3240EZ-ND	Digi-Key	2	\$2.54	\$5.08
36	Voltmeter	ASIN B00NQ87J7A	Amazon	1	\$9.85	\$9.85
					Total Price	\$969.67

Figure 3.3.1: The materials I used to construct my the electronics portion of my interferometer including part number and manufacturer. The numbers in the left hand column will be used in the image and throughout the chapter when referencing a part.

3.3.2 Methods

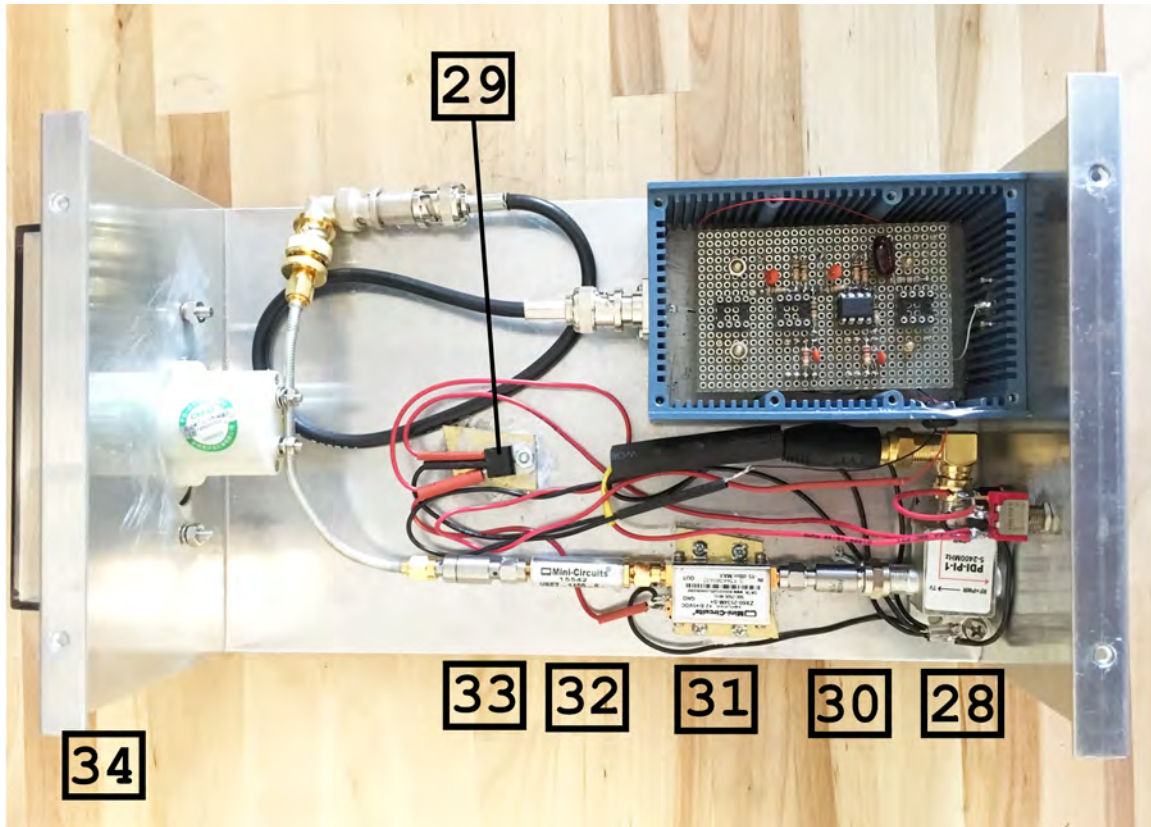


Figure 3.3.2: An image of the inside of electronic box used to adjust radio signal. Each component has been labeled and will be referenced throughout the chapter.

As mentioned, two of the mirrors mounted near the ends of the ladder collect signal and send it toward the mirrors centrally located along the ladder. These two mirrors direct the signal toward the parabolic dish, perfectly shaped to focus the signal toward the Low Noise Block Feedhorn [23]. At this point, the signal has been collected as an electrical signal. The only remaining step is to adjust this signal to be within the appropriate specifications to be legible to our LabPro analog to digital (A/D) converter [25] [26]. The electronic equipment responsible for adjusting the signal is located in a 10" × 6" aluminum box [34]. The radio signal from the sun has a frequency between 10-13 GHz. The goal is to isolate the range of frequency we are most interested in and then adjust the

amplification of this signal to cover the range from 0 to +6 Volts DC to be interpreted by the differential voltage probe LabPro add on [27].

First, the signal encounters the LNBF, which is positioned at the focus of the parabolic dish. The LNBF functions to down convert the frequency of the signal. This is achieved by creating a beat frequency. Mixing the received signal with a generated signal at a slightly offset frequency, a signal with a much lower frequency can be gleaned. The resulting signal has frequencies between 0.950-1.950 GHz, and the process is known as heterodyne mixing. The new signal exits the LNBF through an F connector and travels down a coaxial cable toward the rest of the box.

In order to generate a signal to beat against, the LNBF requires a 24 volts DC. This current is traveling up the through the same coaxial cable from the box toward the LNBF. This current is supplied by the first element of the box, a power inserter [28].

Twenty-four Volts DC is supplied to the box from a power generator or motorcycle battery [2] for portability. Once inside of the box, this power is connected to a single throw double pole switch, then distributed directly to the power inserter through an F connector and also to a 5 volt power inverter [29]. Five volts DC will be distributed to several locations in the electronic box.

The signal flows through an ohm adaptor [30] which adjusts the resistance the current encounters so that impedance are well matched. Impedance matching appeared as a strange and convoluted concept to me at first, so I have included a short explanation for curiosity's sake. A radio signal entering the LNBF has a specific impedance that must be assimilated to an electronic system with its own specific impedance. For the maximum power of the signal to be preserved, the impedance of the load, here the electronic box, should be equal to the complex conjugate of the source impedance, the radio signal. For low-frequency DC signals, if the source and load resistances are equal, their impedances

will be complex conjugates of each other, and maximum power will be transferred through the system. By adjusting the resistance of the source signal from 75 Ohms to 50 Ohms, power transfer is maximized through the system.

After passing through the ohm adaptor, the signal passes through an amplifier [31] then enters the band-pass filter [32], analogous to a pasta strainer, but for frequencies. The band-pass filter allows signal with frequencies between 1.35 GHz and 1.45 GHz to pass and eliminates any signal outside of this range. A spectrum analyzer can be used to determine the best bandpass zone is for any radio source. For our Sun, the range is between 1.35 GHz and 1.45 GHz.

At this point, our AC current is alternating in polarity. If this signal were to enter the A/D converter and be read directly, the two polarities would cancel each other and the total power would be zero. The square-law detector diode [33] only passes signal in one direction and therefore deletes half of the incoming signal. The orientation of the square-law detector determines whether the the positive or negative portion of the signal can pass. This square-law detector is a very expensive piece of equipment. The diode is used here to convert the AC signal to a DC signal, which is easier to manipulate and amplify compared to a high frequency AC signal. The device is not essential, and due to cost, I encourage experimenting without the square-law detector. This would require building an amplifier for AC current. A 1 GHz AC signal is difficult to deal with and may lead to design difficulties, but accurate data could be collected without a square-law detector.

The signal passes through my custom made variable direct coupled DC amplifier [38] to adjust the total power to span from 0 to 6 Volts DC. A similar interferometer system [koda1995interfer] uses two attenuators and one amplifier to adjust the amplitude of the signal earlier in the setup. I thought this setup seemed too specifically tailored to measure the diameter of the Sun. To examine a different source the entire system of am-

plifiers and attenuators would have to be replaced and reconfigured. With my adjustable amplifier a dial can quickly substitute different resistors and adjust the gain to fit within the 0 to 6 Volt range. Figure 3.3.3 shows two diagrams of the system I have built. The total gain of the system is determined by $\frac{R_F}{R_G}$, two resistors within the circuit.

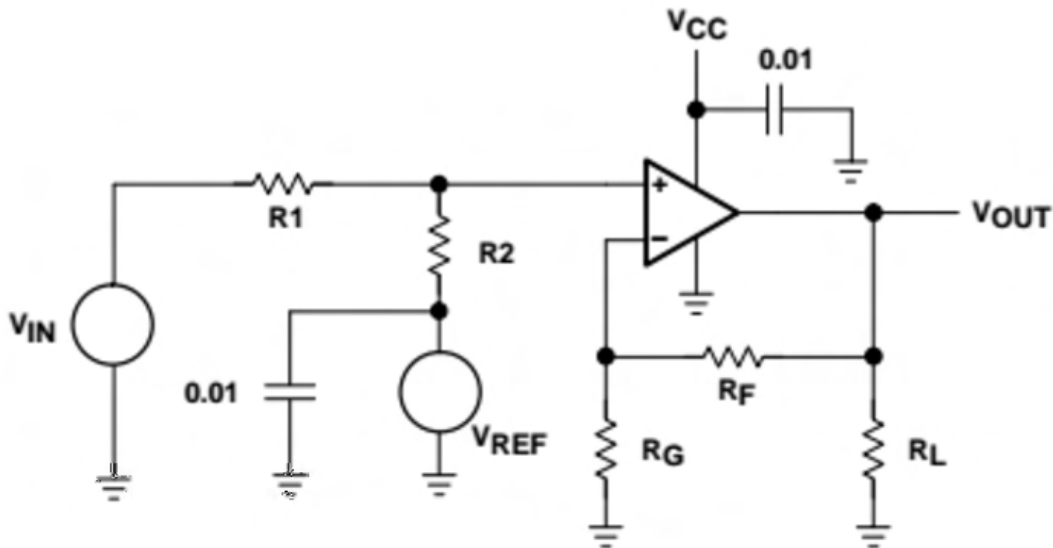


Figure 3.3.3: This circuit board schematic shows the system I replicated in my variable DC amplifier. More information regarding this system can be found in Single-Supply Op Amp Design Techniques Manual by Texas Instruments [25]. This image was originally printed on page 8 of the manual.

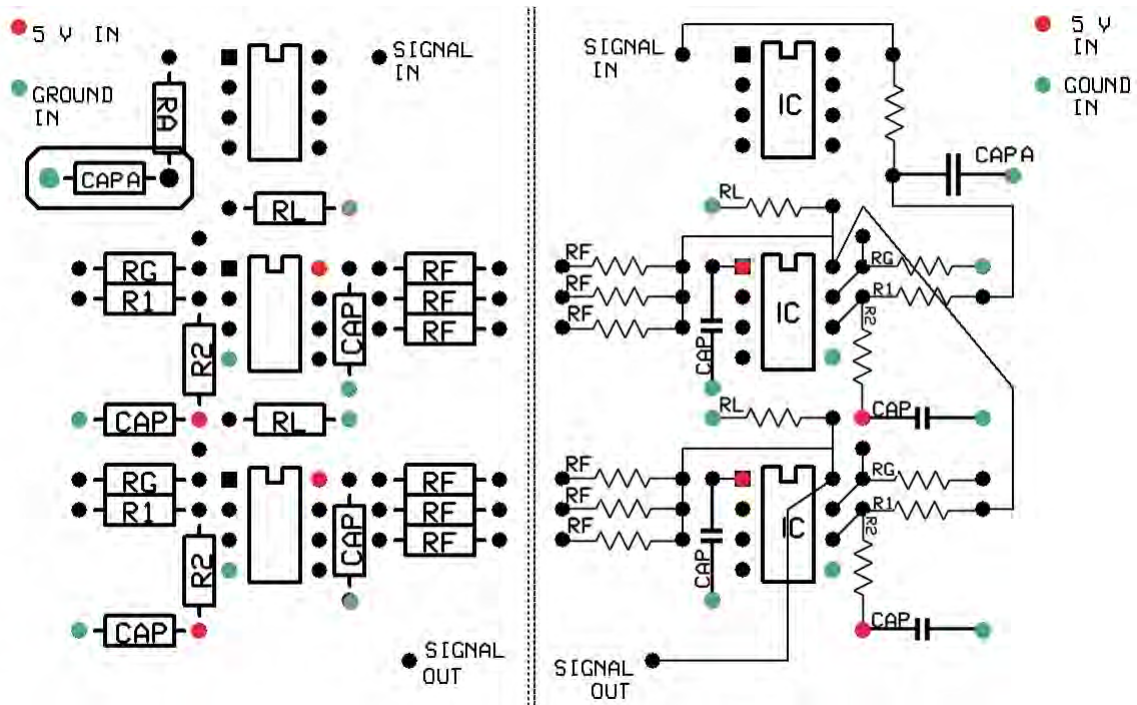


Figure 3.3.4: This circuit board diagram shows the components used in my variable DC amplifier. The circuit board diagram on the right shows the wiring used in the variable DC amplifier. If the system is to be built on a blank circuit board, each dot signifies the location of a soldered conducting post. The components can then be soldered to the posts. The red posts should be connected to 5 V DC and the green posts should be connected to ground.



Figure 3.3.5: Here is an in progress photo of my variable operational amplifier. This images shows the same side as the right side of Figure 3.3.3.

The system is always picking up noise and it is useful to continually remove unwanted signal. For example, every wire in the DC converter functions as an antenna. The first resistor and capacitor, labeled RA and CAPA, function as a low-pass filter passing any signal below 20 KHz, and sending any signal above this frequency to ground. 20 KHz is an arbitrary cut off. Audio noise is near this range, and that is what I imagined as a noise source and wanted to send to ground. The capacitor stores energy below 20 KHz then releases the energy in a way that decreases the ripple of the DC signal.

The current is amplified by the system using CA3240 integrated circuit [35] by a gain of $\frac{RF}{RG}$. The system will have a multi-position switch to flip between different RF resistors to adjust the gain of the system. I have designed the system to have two rounds of amplification for more options of gain. Two rounds of amplification with lower gain adds less noise than one round of a larger gain. The capacitors labeled CAP function to remove noise. Again, the power supply wires gather noise as they travel to the IC. These capacitors send any signal that is not DC to ground while allowing any DC signal to pass. At last, the signal is exported to a Lab Quest 2 using a differential voltage probe add-on.

4

The Signal

The Sun is best known and respected as a source of visible light. Interestingly, it is also a powerful radio source. Radio astronomy has been vital to locating the layers of the Sun's atmosphere and exploring processes that occur within the Sun. I begin this chapter with an overview of the origins of the Sun's radio emissions to show why solar radio study is enlightening and relevant. Understanding the diverse radio emissions of the Sun will further justify the design of my radio interferometer. In Section 4.2 I will depict my progress in testing my interferometer and in Section 4.3, I will delineate future goals for the project.

4.1 Radio Emission of The Sun

The Sun's atmosphere is divided into three major zones, the photosphere, chromosphere and corona. The photosphere is a thin layer responsible for the Sun's emissions in the visual spectrum. The inner limit of the photosphere is somewhat arbitrary, but defined to be 100 km below where light with wavelength 500nm can be seen [9]. The boundary

between the photosphere and chromosphere is defined where the sun becomes invisible. This boundary point is also identified by a temperature minimum of 4400 °K.

The chromosphere is the layer of the Sun's atmosphere that extends 2×10^4 km above the photosphere. The temperature of the chromosphere gradually increases with increasing altitude.

A dramatic temperature shift to 10^6 °K signifies the boundary from the chromosphere into the corona, the outermost shell of the Sun's atmosphere. The corona's energy output is on the order of 10^6 times less than the energy output of the photosphere [9]. The density of particles is so low in the corona that it is transparent to most electromagnetic radiation besides radio waves. The density of particles in the corona is 10^{15} particles m^{-3} where the density of solar wind particles near the Earth is roughly 10^7 particles m^{-3} .

The corona and chromosphere are inhomogeneous, and both emit in the radio spectrum. Their radio emissions can be divided into the three categories of catastrophic events, steadily variable emissions, and quiet sun emissions. The catastrophic portion of radio emissions consist of dramatic and sporadic episodes that are almost always associated with solar flares. These catastrophic events can claim the radio noise Karl Jansky observed in 1930 [6]. Then there is the slowly varying component of radio emissions, waning and waxing in a predictable fashion. Remaining is the quiet, reliable and steady radio emissions from the quiet sun.

Most of the action occurring on the surface of the Sun is due to disturbances in the Sun's magnetic field. The magnetic field of the Sun exists in the photosphere and lower chromosphere. The magnetic field flows with the plasma, which doesn't rotate at a steady rate. For example, the equatorial line completes one rotation every 27 days, while 70 °N latitude completes one rotation every 33 days [6], which is known as differential rotation. In some occurrences, the magnetic field tangles around itself creating massive

amounts of energy just below the surface of the photosphere. This event appears as a dark spot in the photosphere called a sunspot. The most central dark spot is called the umbra, while the surrounding dim area is called the penumbra. The strength and polarity of the magnetic field near a sunspot can be found by the Zeeman effect. Spectral lines from appear to be split as the magnetic field “removes the degeneracy inherent in atomic energy levels” [9]. Effects from the entanglement of the magnetic fields extend into other levels of the Sun’s atmosphere.

If energy built up in a knot in the Sun’s magnetic field is released quickly, a flare is created directly above a sunspot in the upper chromosphere to lower corona. Particles are shot with immense amounts of energy, as much as 10^{25} Joules, in arc like shapes. During a solar flare “showers of brilliant gas shoot up and cascade downwards at speeds of 200 miles per second” [6] and can reach 100,000 km in length. As particles, mostly protons and helium nuclei, are shot through the atmosphere, they release energy in the radio spectrum by synchrotron radiation.

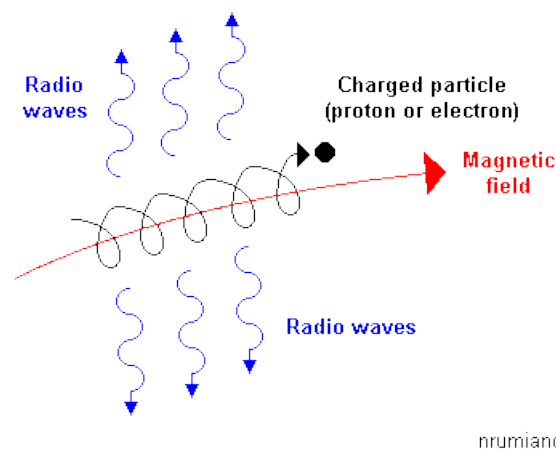


Figure 4.1.1: Synchrotron radiation is a process that occurs in the Sun where charged protons emit radio waves.

When a relativistic electron with charge q is traveling through a magnetic field B with velocity v , the force on the electron is described by

$$F = q(v \times B). \quad (4.1.1)$$

The velocity component parallel to the magnetic field is undisturbed while the velocity component perpendicular to the magnetic field lines is forced into a circular orbit around the lines. The electron proceeds in a helical path, accelerating and releasing energy as radio waves [9]. Radio emission during a flare can reach up to a million times the brightness observed from typical solar radio emission and the event can last several minutes [6].

Longer flares that occur at lower frequencies are labeled ‘noisestorms.’ A noisestorm is any solar flare that occurs on the time scale of days at frequencies below 500 MHz [6]. The origins of these flares are not fully understood.¹

The slowly variable component (SVC) of the Sun’s radio emissions gives insight into the terrain of the Sun’s surface. This data has helped to depict the 27-day rotation period of the Sun and shows expected peaks near known sunspot locations. Slowly variable radio emissions have contributed to uncovering the 11.3 year cycle of sunspot activity by meshing data together and identifying the rate of repetitive patterns. The 11.3 year cycle is distinct, but the Sun’s luminosity seems to fluctuate over longer times scales as well. For example, the period between 1645 and 1715, called the Maunder minimum, showed solar luminosity a few tenths of a percent lower than average [9].

As mentioned before, rotational consistency of the Sun is unreliable at best. Radio emissions have identified that the three layers of the Sun rotate at different rates. Two differing rotation rates converge to a shell known as the tachocline. The shear created by

¹To produce such powerful eruptions in the chromosphere, the epicenter of the flare would need to reach temperatures of 10^8 °K, a temperature beyond the thermal emissions of hot gasses.

conflicting rates of rotation causes electric currents within the plasma at the tachocline, which may be the origin of the Sun's powerful magnetic field [9]. The slowly variable component of the Sun's radio emissions predominately exist above 500 MHz and can be explained by "coronal condensation" [6]. Coronal condensation is a pocket of high temperature and density in the corona that resides directly above a sunspot. SVC emissions are predominately used to identify and capture other elusive patterns of the Sun.

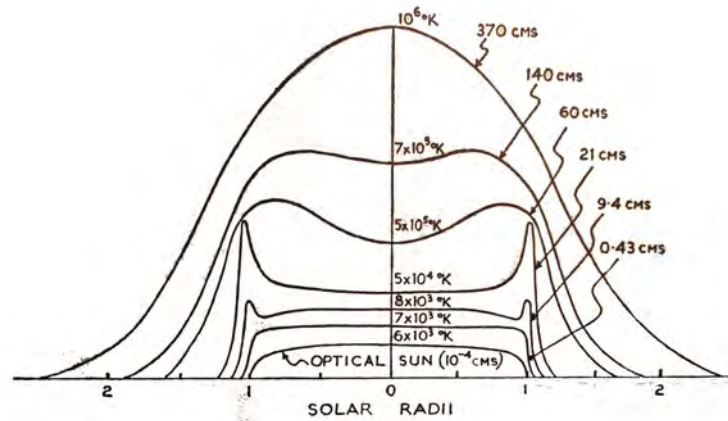


Figure 4.1.2: The radio brightness distribution across the equator of the Sun at six frequencies in the range of .43 cm to 370 cm. The optical Sun is shown for comparison. [6]

After removing SVC and solar flares, we are left with the quiet solar emissions. When gas particles collide with each other, electrons of the particles lose energy in the form of a photon. A more powerful collision releases more energy in the form of a photon with higher wavelength. The energy of a photon E is related to its wavelength λ by Plank's equation

$$E = \frac{hc}{\lambda}. \quad (4.1.2)$$

where h is Plank's constant and c is the speed of light. Gas particles in the corona are sparse and it is uncommon for two particles to experience a full collision. Particles merely brush near each other and cause minor energy releases as a photon with wavelength between 1 cm and 20 cm [9]. Lower wavelengths are emitted as the atmosphere becomes more dense near the photosphere. Figure 4.1 depicts how "the brightness as well as the

shape of the Sun alters markedly from one frequency to the next” [6]. Looking at lower frequency signals shows more of the corona, which has a larger radius and more elliptical shape than the photosphere. Denisse, Blum and Steinberg [31] mapped the sun at 169 MHz and found the semi-major axis to be 1.3 times the semi-minor axis. My interferometer system is designed to operate in the high frequency range between 10 GHz and 13GHz, associated with a wavelength between 2.3 cm and 3 cm. In this zone, radio emission occurs in the lower chromosphere at nearly the same radius as the optical diameter of the Sun.

Explorations of the radio spectra emanating from the sun are capable of revealing phenomena that are indecipherable using visual spectra data alone. Solar radio data often appears unrelated to visual data, and reveals important non-thermal processes in the Sun [6]. Solar radio observations are leading to advances in information regarding the Sun’s atmosphere. Most notably radio studies help to understand and observe the slowly varying components of the Sun’s structure, [6] provide information about fully ionized plasmas, inform the understanding of massive solar eruptions, improve the capabilities of radio technology, and explore it’s applications in astrophysics [6].

4.2 Testing the Signal

After constructing the electronics equipment, I needed a method to test the signal. In the United States, satellite television functions over the same frequency bands as the Sun’s emissions. Stations are broadcast between 11.7 and 17.8 GHz. I gained access to satellite television signals and then connected the function analyzer to the circuit in between the diode and DC amplifier. The function analyzer showed several bandwidths of signal (corresponding to different television stations). The amplitudes of the signals were in the shape of a bell curve between 1.35 and 1.45 GHz. This indicated that the bandpass filter was functioning correctly.

Since satellite television exists over a wider band of frequencies than the Sun's emissions, I could not be certain whether the signal on the function analyzer would be within the range of solar emissions. At this point, it was unclear whether the entire system was functioning properly. There exist highly specialized function generators capable of creating a 10 GHz signal, but they cost nearly \$25,000.

I was shown a DIY article² [29] that detailed the manipulation of a miniature motion sensor into a 10 GHz generator. The motion sensor, the ST Electronics HB100.2, costs around \$4.00 and the generator can be constructed for under \$25.00. Amateur astronomer Jeff Wadsworth methodically explains the required materials and procedure. Basically, the steps are to “add power, run a coax line from the transmit feed network in the HB100 to an SMA connector, put it all in a plastic box [with a control switch] and adjust the frequency” [29]. When pointed at the satellite dish, a distinct peak could be seen on the function generator within the bandpass. This indicates the system is functioning properly through the diode.

4.3 Future Goals

While my interferometer is well on its way toward completion, there are a few kinks that need ironing. Two motors have recently been delivered but not yet installed. These motors are to be directed by a manually operated rocker switch which controls a delivery of current. This would be a rudimentary system, but the interferometer could be moved with minimal labor. Ideally, the motors would have a computerized control system capable of slight movements along a highly specified path. Open source programs³ exist to precisely direct the motors to follow a source across the sky as the earth rotates. This would enable more advanced and accurate data collection capabilities. Eventually, I would like to survey

²special thanks to Richard Murphy for his expertise during this step

³Various open source programs and relevant information can be found at <http://www.bbastrodesigns.com/StepperSystem.html>

solar radio emission over longer periods of time, possibly branching into the slowly varying component of the Sun's emissions. I also hope to paint my interferometer or maybe etch my name into its side.

Bibliography

- [1] Hans J Witt and Shude Moa, *On the minimum magnification between caustic crossings for microlensing by binary and multiple stars*, The Astrophysical Journal Letters **447** (1995), no. 2, L105.
- [2] Scott B Gaudi, *Microlensing surveys for exoplanets*, Annual Review of Astronomy and Astrophysics **50** (2012), 411–453.
- [3] Edwin F and Wheeler Taylor John Archibald, *Spacetime physics*, Macmillan, 1992.
- [4] Jin Koda and James Barrett and Gene Shafto and Jeff Slechta and Tetsuo Hasegawa and Masahiko Hayashi and Stanimir Metchev, *A Michelson-type radio interferometer for university education*, American Journal of Physics **84** (2016), no. 4, 249–256.
- [5] Peter Schneider and Achim Weiss, *The two-point-mass lens-Detailed investigation of a special asymmetric gravitational lens*, Astronomy and Astrophysics **164** (1986), 237–259.
- [6] R.D. Davies and H.P. Palmer, *Radio Studies of the Universe*, Routledge and Kegan Paul Limited, Frome and London, 1959.
- [7] Hans J Witt and Shude Mao, *On the minimum magnification between caustic crossings for microlensing by binary and multiple stars*, The Astrophysical Journal Letters **447** (1995), no. 2, L105.
- [8] Gary and Fischer Bernstein Philippe and Tyson, *Improved parameters and new lensed features for Q0957+ 561 from WFPC2 imaging*, The Astrophysical Journal Letters **483** (1997), no. 2, L79.
- [9] Bradley W. Carroll and Dale A. Ostlie, *An Introduction to Modern Astrophysics*, Pearson Education Inc, San Francisco, California, 2007.
- [10] Bohdan Paczynski, *Gravitational microlensing by the galactic halo*, The Astrophysical Journal **304** (1986), 1–5.
- [11] Hans J Witt and Shude Mao, *Can lensed stars be regarded as pointlike for microlensing by MACHOs?*, The Astrophysical Journal **430** (1994), 505–510.

- [12] Arlie O. Petters and Harold Levine and Joachim Wambsganss, *Singularity theory and gravitational lensing*, Vol. 21, Springer Science & Business Media, 2012.
- [13] Michael A Garrett, *Radio astronomy transformed: Aperture arrays? Past, present and future*, AFRICON, 2013, 2013, pp. 1–5.
- [14] Albert Einstein, *Lens-like action of a star by the deviation of light in the gravitational field*, Science **84** (1936), no. 2188, 506–507.
- [15] Fritz Zwicky, *On the probability of detecting nebulae which act as gravitational lenses*, Physical Review **51** (1937), no. 8, 679.
- [16] Arthur S Eddington, *The internal constitution of the stars*, The Scientific Monthly (1920), 297–303.
- [17] Dennis and Carswell Walsh Robert F and Weymann, *0957+ 561 A, B- Twin quasis-tellar objects or gravitational lens*, Nature **279** (1979), no. 5712, 381–384.
- [18] Silvia and Roulet Mollerach Esteban, *Gravitational lensing and microlensing*, World Scientific, 2002.
- [19] Vesto M Slipher, *Spectrographic observations of nebulae*, Popular astronomy **23** (1915), 21–24.
- [20] Willem De Sitter, *Einstein's theory of gravitation and its astronomical consequences. Third paper*, Monthly Notices of the Royal Astronomical Society **78** (1917), 3–28.
- [21] Edwin Hubble, *A relation between distance and radial velocity among extra-galactic nebulae*, Proceedings of the National Academy of Sciences **15** (1929), no. 3, 168–173.
- [22] Jacob K Luhn and Matthew T Penny and B Scott Gaudi, *Caustic Structures and Detectability of Circumbinary Planets in Microlensing*, The Astrophysical Journal **827** (2016), no. 1, 61.
- [23] David J and Osborn Armstrong Hugh P and Brown, *On the abundance of circumbinary planets*, Monthly Notices of the Royal Astronomical Society **444** (2014), no. 2, 1873–1883.
- [24] Sun Hong Rhie, *How Cumbersome is a Tenth Order Polynomial?: The Case of Gravitational Triple Lens Equation*, arXiv preprint astro-ph/0202294 (2002).
- [25] *Single-Supply Op Amp Design Techniques*, available at <http://www.ti.com/lit/an/sloa030a/sloa030a.pdf>.
- [26] Ian A and Udalski Bond A and Jaroszyński, *OGLE 2003-BLG-235/MOA 2003-BLG-53: a planetary microlensing event*, The Astrophysical Journal Letters **606** (2004), no. 2, L155.
- [27] William Reush, *Visible and Ultraviolet Spectroscopy*, <https://www2.chemistry.msu.edu/faculty/reusch/virttxtjml/spectrpy/uv-vis/spectrum.htm>.
- [28] S Hawking, *The Illustrated Theory of Everything*, Phoenix Books, Beverly Hills, 2003.
- [29] Jeff Wadsworth, *\$25 10GHz Signal Generator*, QEX (May/June 2015), 34–38.
- [30] NASA, *Exoplanet Exploration*, December 16, 2015.
- [31] EJ and Denisse Blum JF and Steinberg, *Radio astronomy at the Meudon Observatory*, Proceedings of the IRE **46** (1958), no. 1, 39–43.

.1 One Lens Light Curve from Image Positions

Single Lens Equation (2.1.1)

$$u[y_] := y - (1/y)$$

(1/det J) Equation (2.1.6)

$$f[y_] := \left(\frac{1}{1 + \frac{1}{y^2}} \right) \left(\frac{y}{u} \right)$$

Onelens block will produce total magnification as a function of T, which is defined as $((t-t_0)/t_e)$ in Section 1.5. The lens equation, $u[y]$, and $1/\det J$, $f[y]$, are input, and magnification as a function of u_0 and T, $A[T,u_0]$, is output. The manipulate function is invoked for the u_0 parameter.

```

onelens[lenseq_, jacobian_] := Block[{sol, y, u, table, red, magu, j, magr},
  sol = NSolve[lenseq == u, {y, y1}];
  jac = jacobian /. sol;
  magu = Total[Abs[jac]];
  magr = magu /. u -> Sqrt[(u0^2) + (T^2)]
p[T_, u0_] := Evaluate[onelens[u[y], f[y]]]
Manipulate[Plot[p[T, u0], {T, -2, 2},
  AxesLabel -> {T, Magnification}, PlotRange -> {{-2, 2}, {0, 6}}, {u0, 0, 2}]

```


.2 One Lens Finite Source

A spherical star with uniform brightness and radius r is defined as

$$\begin{aligned}\xi[\varphi] &= r e^{i\varphi} + \xi_0 \\ r &= .1; \\ u_0 &= 0;\end{aligned}$$

and the total magnification by separating the complex part from the real part, then taking the ratio of the total area of each image to the total area of the source.

$$\begin{aligned}x1[\varphi] &:= ((r \cos[\varphi] + (\text{Sqrt}[(u_0)^2 + T^2])) / 2) \\ &\left(1 - \sqrt{1 + \frac{4}{((u_0)^2 + T^2) + (2r (\text{Sqrt}[(u_0)^2 + T^2]) \cos[\varphi] + r^2)}} \right) \\ x2[\varphi] &:= ((r \cos[\varphi] + (\text{Sqrt}[(u_0)^2 + T^2])) / 2) \\ &\left(1 + \sqrt{1 + \frac{4}{((u_0)^2 + T^2) + (2r (\text{Sqrt}[(u_0)^2 + T^2]) \cos[\varphi] + r^2)}} \right) \\ y1[\varphi] &:= ((r \sin[\varphi]) / 2) \left(1 - \sqrt{1 + \frac{4}{((u_0)^2 + T^2) + (2r (\text{Sqrt}[(u_0)^2 + T^2]) \cos[\varphi] + r^2)}} \right) \\ y2[\varphi] &:= ((r \sin[\varphi]) / 2) \left(1 + \sqrt{1 + \frac{4}{((u_0)^2 + T^2) + (2r (\text{Sqrt}[(u_0)^2 + T^2]) \cos[\varphi] + r^2)}} \right)\end{aligned}$$

Below I find the total magnification, A_{total} , as a function of T defined as $(t - t_0) / t_e$. I have placed the A_{total} function inside of a `ListPlot` and iterated over different values of T to create a light curve with with specified impact parameter, u_0 , and radius, r .

```
In[8]:= (*A1=((1/(Pi r^2))NIntegrate[ (y1[\varphi] D[x1[\varphi],\varphi]),{\varphi,0,(2 Pi)}])*)
```

```
In[9]:= (*A2=((1/(Pi r^2))NIntegrate[ (y2[\varphi] D[x2[\varphi],\varphi]),{\varphi,0,(2 Pi)}])*)
```

```
In[10]:= (*Atotal=A1-A2*)
```

```
ListPlot[Table[{T, ((1 / (Pi r^2)) NIntegrate[ (y1[\varphi] D[x1[\varphi], \varphi]), {\varphi, 0, (2 Pi)}]) -
((1 / (Pi r^2)) NIntegrate[ (y2[\varphi] D[x2[\varphi], \varphi]), {\varphi, 0, (2 Pi)}])}], {T, -2, 2, .001}],
AxesLabel -> {T, Magnification}, PlotRange -> {{-2, 2}, {0, 20}}
```


.3 Double Lens

The variable d refers to Delta M.

The star is within the caustic under the condition $(z1)^2 < 2m$.

```

d = 0;
pi = 1;

In[5]:= c0 = ((z1)^2) * ((4 (d^2) z) + (4 m d (z1)) + (4 d (z^2) (z1)) +
(2 * m * z * (z1)^2) + ((z^3) * (z1)^2) - (2 d (z1)^3) - (z * (z1)^4));

In[6]:= c1 = (-8 d m z (z1)) - (4 (d^2) (z1)^2) - (4 * (m^2) * ((z1)^2)) -
(4 (z^2) * m * (z1)^2) - (4 d z ((z1)^2)) - ((z^2) * (z1)^4) + ((z1)^6);

In[7]:= c2 = 4 (m^2) z + (4 m d (z1)) - (4 d (z^2) (z1)) - (2 (z^3) ((z1)^2)) + (4 d ((z1)^3)) + 2 z * (z1)^4;

In[8]:= c3 = 4 m (z^2) + (4 d (z1) z) + 2 (z^2) * (z1)^2 - 2 (z1)^4;

In[9]:= c4 = (-2 m * z) + (z^3) - (2 d (z1)) - (z * (z1)^2);

In[10]:= c5 = (z1)^2 - z^2;

In[11]:= g1[z_] := (c0) + (c1) * z + (c2) * (z^2) + (c3) * (z^3) + (c4) * (z^4) + (c5) * (z^5);

In[12]:= g2[z_] =
A * pi * (1 - (m^2) ((1 / (z1 - z) + (m / (z1 - z)) + (m / (-z1 - z)))^2) + (1 / (-z1 - z) + (m / (z1 - z)) +
(m / (-z1 - z)))^2) ((1 / (z1 - z)^2) + (1 / (-z1 - z)^2)) - 1;

In[14]:= f[A_] := Resultant[g1[z], g2[z], z]

In[15]:= f[A]

Out[15]= (-281 474 976 710 656 - 4 503 599 627 370 496 A - 3 764 727 813 505 024 A^2 + 7 124 835 347 988 480 A^3 +
3 710 851 743 744 000 A^4 - 3 710 851 743 744 000 A^5 + 562 949 953 421 312 z^2 + 6 192 449 487 634 432 A z^2 -
18 788 454 695 436 288 A^2 z^2 - 2 533 274 790 395 904 A^3 z^2 - 29 033 704 043 053 056 A^4 z^2 +
29 033 704 043 053 056 A^5 z^2 - 281 474 976 710 656 z^4 + 844 424 930 131 968 A z^4 +
35 571 400 181 809 152 A^2 z^4 - 60 693 041 853 235 200 A^3 z^4 + 83 865 249 408 614 400 A^4 z^4 -
83 865 249 408 614 400 A^5 z^4 - 2 251 799 813 685 248 A z^6 - 1 829 587 348 619 264 A^2 z^6 +
73 253 862 688 948 224 A^3 z^6 - 103 310 112 545 832 960 A^4 z^6 + 103 310 112 545 832 960 A^5 z^6 -
281 474 976 710 656 A z^8 - 9 183 121 115 185 152 A^2 z^8 + 4 292 493 394 837 504 A^3 z^8 +
36 712 693 251 440 640 A^4 z^8 - 36 712 693 251 440 640 A^5 z^8 - 1 899 956 092 796 928 A^2 z^10 -
16 184 811 160 862 720 A^3 z^10 + 18 959 978 509 369 344 A^4 z^10 - 18 959 978 509 369 344 A^5 z^10 -
105 553 116 266 496 A^2 z^12 - 4 749 890 231 992 320 A^3 z^12 - 6 599 268 789 911 552 A^4 z^12 +
6 599 268 789 911 552 A^5 z^12 - 492 581 209 243 648 A^3 z^14 - 3 667 970 790 260 736 A^4 z^14 +
3 667 970 790 260 736 A^5 z^14 - 17 592 186 044 416 A^3 z^16 - 594 835 790 626 816 A^4 z^16 +
594 835 790 626 816 A^5 z^16 - 41 781 441 855 488 A^4 z^18 + 41 781 441 855 488 A^5 z^18 -
1 099 511 627 776 A^4 z^20 + 1 099 511 627 776 A^5 z^20) / ((-4096 + 4096 z)^2 (4096 + 4096 z)^2)

In[17]:= q[resultant_] := Block[{u0, magu, table, a, img, magr}, img = NSolve[resultant == 0, A];
table = Table[i, {i, 1, Length[img]}];
a = A /. img[table];
magu = Total[Abs[a]];
magr = magu /. z -> Sqrt[(mu0^2) + (T^2)]

In[18]:= p[T_, mu0_] := Evaluate[q[f[A]]]

In[19]:= Manipulate[Plot[p[T, mu0], {T, -5, 5},
AxesLabel -> {T, Magnification}, PlotRange -> {{-5, 5}, {0, 50}}, {mu0, .2, 2}]

```


.4 Triple Lens

Polynomial One

```

a = -(x1 + x2 + x3);
b = (x1 x2 + x1 x3 + x2 x3);
c = -(x1 x2 x3);
d = (e1 x2 x3 + e2 x1 x3 + e3 x2 x1);
aω = ((Conjugate[ω] - Conjugate[x1]) +
      (Conjugate[ω] - Conjugate[x2]) + (Conjugate[ω] - Conjugate[x3]));
bω = (((Conjugate[ω] - Conjugate[x1]) (Conjugate[ω] - Conjugate[x2])) +
      ((Conjugate[ω] - Conjugate[x2]) (Conjugate[ω] - Conjugate[x3])) +
      ((Conjugate[ω] - Conjugate[x3]) (Conjugate[ω] - Conjugate[x1])));
cω = ((Conjugate[ω] - Conjugate[x1]) (Conjugate[ω] - Conjugate[x2])
      (Conjugate[ω] - Conjugate[x3]));
dω = ((e1 (Conjugate[ω] - Conjugate[x2]) (Conjugate[ω] - Conjugate[x3])) +
      (e2 (Conjugate[ω] - Conjugate[x1]) (Conjugate[ω] - Conjugate[x3])) +
      (e3 (Conjugate[ω] - Conjugate[x2]) (Conjugate[ω] - Conjugate[x1])));

```

My H matrix starts at 1,1 where the coefficients from Rhie 2002 begin at H_{00} so I adjusted my cff[k] function by adding 1 to every index of H. For example H_{23} from Rhie 2002 corresponds to $H[[3,4]]$.

```

cff[k_] := (H[[1, k + 1]] + (H[[2, k + 1]] (aω)) + (H[[3, k + 1]] (bω)) + (H[[4, k + 1]] (cω))) -
  ((H[[1, k + 2]] ω + H[[1, k + 2]] ((aω ω) - 1)) +
   (H[[3, k + 2]] ((bω ω) + aω - Conjugate[ω])) + (H[[4, k + 2]] ((cω ω) + bω))) /. conjless

H = {
  {0, d^3, 3 a d^2, 3 a^2 + 3 d^2, a^3 + 6 a d, 3 a^2 + 3 d},
  {0, c d^2, 2 a c d + b d^2, a^2 c + 2 a b d + 2 c d + a d^2, a^2 b + 2 a c + 2 a^2 d + 2 b d + d^2, a^3 + 2 a b + c +},
  {0, c^2 d, a c^2 + 2 b c d, 2 a b c + c^2 + b^2 d + 2 a c d, a b^2 + 2 a^2 c + 2 b c + 2 a b d + 2 c d, 2 a^2 b + b^2 + 4 a c +},
  {0, c^3, 3 b c^2, 3 b^2 c + 3 a c^2, b^3 + 6 a b c + 3 c^2, 3 a b^2 + 3 a^2 c +}
}

R1[z_] := Sum[(cff[k] z^k), {k, 0, 10}]

```

Polynomial Two

```

In[31]:= pi = 1;
p = ((x1 - z)^2);
q = ((x2 - z)^2);
r = ((x3 - z)^2);
s = (((Conjugate[x1] + (Conjugate[ω] - (e1 / (x1 - z)) - (e2 / (x2 - z)) - (e3 / (x3 - z))))^2);
t = (((Conjugate[x2] + (Conjugate[ω] - (e1 / (x1 - z)) - (e2 / (x2 - z)) - (e3 / (x3 - z))))^2);
v = (((Conjugate[x3] + (Conjugate[ω] - (e1 / (x1 - z)) - (e2 / (x2 - z)) - (e3 / (x3 - z))))^2);
g = ((e1 ((x2 - z)^2) ((x3 - z)^2)) + (e2 ((x1 - z)^2) ((x3 - z)^2)) + (e3 ((x1 - z)^2) ((x2 - z)^2));

f[z_] := (- (s t v p q r) + (μ pi s t v p q r) - (μ pi ((e1 t v g) + (e2 s v g) + (e3 s t g))))

```

Series expansion of Polynomial Two to find well ordered thirteenth order polynomial in z.

```
R2[z_] := Series[f2[z], {z, 0, 13}]
```